# Laser-beam powder bed fusion of cost-effective non-spherical hydride-dehydride Ti-6Al-4V alloy

Mohammadreza Asherloo [a], Ziheng Wu [b], Melody H. Delpazir [a], Eyob Ghebreiesus [a], Sara Fryzlewicz [c], Runbo Jiang [b], Benjamin Gould [d], Mike Heim [e], Dave Nelson [e], Mike Marucci [f], Muktesh Paliwal [f], Anthony D. Rollett [b], Amir Mostafaei [a, *]

[a] Department of Mechanical, Materials and Aerospace Engineering, Illinois Institute of Technology, 10 W 32nd Street, Chicago, IL 60616, USA

[b] Department of Materials Science and Engineering, Carnegie Mellon University, Pittsburgh, PA, 15213, USA

[c] Department of Computer Science, Illinois Institute of Technology, 10 W 31st Street, Chicago, IL 60616, USA

[d] Applied Materials Division, Argonne National Laboratory, Lemont, IL 60439

[e] Nel Pretech Corporation, 8420 183rd Place, Tinley Park, IL 60487, USA

[f] Kymera International - Reading Alloys, Robesonia, PA 19551, USA

* Corresponding author: A. Mostafaei (mostafaei@iit.edu)

## Abstract

Hydride-dehydride (HDH) Ti-6Al-4V powders with non-spherical particle morphology are typically not used in laser-beam powder bed fusion (LB-PBF). Here, HDH powders with two size distributions of 50-120 μm (fine) and 75-175 μm (coarse) are compared for flowability, packing density, and resultant density of the LB-PBF manufactured parts. It is shown that a suitable laser power-velocity-hatch spacing combination can result in part production with a relative density of > 99.5% in LB-PBF of HDH Ti-6Al-4V powder. Size, morphology, and spatial distribution of pores are analyzed in 2D. The boundaries of the lack-of-fusion and keyhole porosity formation regimes are assessed and results showed parts with a relative density of > 99.5% could be LPBF processed at a build rate of 1.5-2 times of the nominal production rates in LPBF machines. The synchrotron x-ray high-speed imaging reveals the laser-powder interaction and potential porosity formation mechanism associated with HDH powder. It is found that lower powder packing density of coarse powder and high keyhole fluctuation result in higher fractions of porosity within builds during the LB-PBF process.

**Keywords**: Additive manufacturing; Process map; Build rate; Porosity; Synchrotron-based dynamic x-ray radiography.

## 1. Introduction

In powder-based metal additive manufacturing (AM), both the feedstock and the 3D-printing processes considerably affect the part integrity and cost of the manufactured components. Spherical powders have been extensively used in LB-PBF machines, and there have been various concerns related to powder (i.e., entrapped gas), processing defects (e.g., pores, spatter, roughness), part quality, and performance. Also, the production of fine powder is expensive which reduces their competitiveness and limits their commercial scale-up. Compared to conventional atomized pre-alloyed powder with spherical morphologies, the direct synthesis of non-spherically shaped powder via chemical and mechanical milling methods results in pore-free particles that are more economically efficient [1–3].

Ti-6Al-4V is one of the most popular alloys in metal AM primarily due to its wide application, e.g., aerospace components and orthopedic implants [4]. Gas atomization (GA) is the primary

powder manufacturing process that supplies powder for the metal AM industry [5]. The standard procedure is extremely energy-intensive and relatively expensive. Therefore, alternative powder production methods are required, which would be cost-effective for being used in metal additive manufacturing. In recent years, many technologies for the production of low-cost Ti-powder have become commercialized [6,7]. The hydride-dehydride (HDH) process is an alternative way to produce Ti-6Al-4V powder by using the brittle nature of titanium hydride. This process has the potential to be much greener and has a significantly lower eco-impact. Compared with GA powder, a lower production cost is the primary advantage that comes with HDH powder; depending on the powder size distribution, the powder cost can be reduced by more than 30 % [8,9]. Additionally, it is possible to eliminate the presence of entrapped gas porosity, which can be inherited by as-built AM components and affect the resulting mechanical performance [5,10]. The HDH powder with non-spherical particle morphology and larger powder size would decrease spattered particles due to the mechanical interlocking characteristics and higher weight compared to gas atomized powder with PSD of <50 um [11].

Replacing GA with HDH powder in AM can be challenging and requires a substantial amount of research to understand the physics of laser-powder interaction, melt pool dynamics, and possible defect formation mechanisms [12]. These challenges are primarily caused by the non-spherical powder morphology. Size control is more difficult with HDH powder owing to its non-spherical morphology; for instance, an elongated particle can pass through a finer sieve with its smallest dimension during the screening process resulting in a powder batch with larger size distribution. This will also affect the packing density in the powder bed of HDH powder. Recently, studies have been conducted to use non-spherical powder in the PBF AM processes. Medina [13] studied the effect of blending HDH titanium powder with spherical one in order to reduce the cost of part production and was able to increase the density of the parts using the double melting in electron beam AM. Li et al. [14] reported on the use of another type of non-spherical powder, i.e., water atomized (WA) powder in LB-PBF. They concluded that GA 316L stainless steel powders yield higher density parts because of lower oxygen content and higher packing density compared to WA. Rogalsky et al. [9] investigated the use of non-spherical WA iron powder in LB-PBF and showed that the poor packing density of this type of powder results in lower laser adsorption and final part density, however, by using a powder layer thickness of 60 µm compared to 40 µm, the impact of packing density on final parts was insignificant. Varela et al. [15] investigated LB-PBF of non-spherical HDH Ti-6Al-4V powder (monomodal particle size distribution with $D_{10}$, $D_{50}$, and $D_{90}$ of 54.9, 72.7, and 88.9 µm) and were able to manufacture parts with a relative density of 98.9 % (using layer thickness of 30 µm, and the optimum process parameter is missing).

There are both fundamental and industrial reasons for understanding how the powder characteristics of the HDH powders (due to differences in powder packing density and powder flowability as compared to spherical particles) may affect the characteristics of thermal profile, microstructure, and defect content as well as cost and speed of production. Here, we choose to use LB-PBF on HDH Ti-6Al-4V powders. The feedstock powder is analyzed to understand how morphology and particle size distribution affect the AM process. Additionally, LB-PBF parameters such as laser power, scan speed, and hatch spacing are optimized to determine a process window with a relative density of > 99.5 % in as-built parts. Density measurements, including Archimedes and segmented 2D optical micrographs, are performed. Synchrotron-based dynamic x-ray radiography visualizes laser-powder interaction and potential porosity formation mechanisms associated with HDH powder. Selected samples are further evaluated for microstructure, phase formation, and porosity.

## 2. Experimental procedures

### *2.1 Feedstock powder*

Ti-6Al-4V feedstock powder with two different mean sizes and particle size distributions (PSD) were supplied by Kymera International - Reading Alloys. Figure 1 showed that both powders had non-spherical morphology characterized by scanning electron microscopy (JEOL 5900LV), and, based on the manufacturer's specification, the particle size distributions were in the range 50-120 µm for the fine powder (Figure 1a,b) and 75-175 µm for the coarse powder (Figure 1c,d). The chemical compositions of the feedstock powders provided by the manufacturer are given in

Table 1 and compared to the nominal Ti-6Al-4V alloy. To acquire the mean size and PSD, a total of ~1,100 HDH powder particles were imaged (using an FEI Aspex Express SEM microscope) to ensure adequate powder statistics, and results are illustrated in Figure 1e. The coarse powder showed monomodal size distribution with powder size of $d_{10}$ = 83 µm, $d_{50}$ = 109 µm, and $d_{90}$ = 142 µm with a mean size of 112 µm and average circularity of 0.46, whereas the fine powder showed a bimodal size distribution with powder size of $d_{10}$ = 28 µm, $d_{50}$ = 82 µm and $d_{90}$ = 103 µm with a mean size of 76 µm and average circularity of 0.68. The flowability of HDH powders was characterized with a Freeman FT4 rheometer; more specifically, the powder-specific energy (SE) and the bulk flow energy (BFE) were measured.

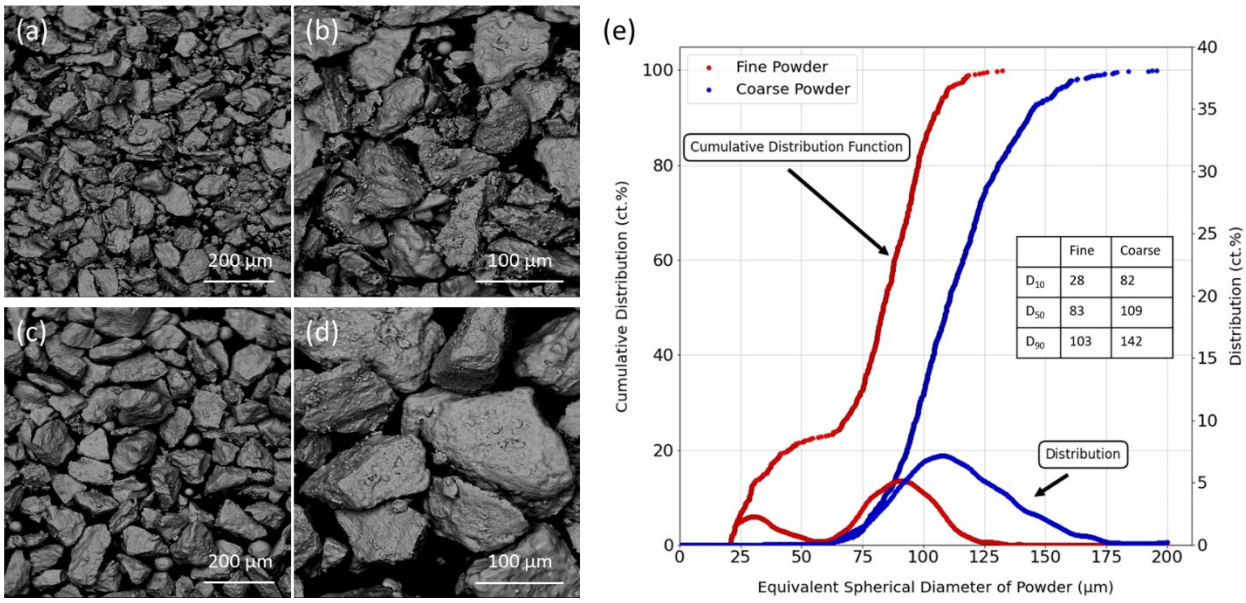


Figure 1. SEM micrographs of the HDH Ti-6Al-4V powders at two magnifications; (a,b) fine powder and (c,d) coarse powder. (e) Particle size distribution measured via SEM image analysis and ImageJ software.

Table 1. Nominal chemical composition of Ti-6Al-4V alloy and the feedstock HDH Ti-6Al-4V powder provided by the manufacturer [wt.%].

| | Ti | Al | V | Fe | C | H | N | O |
|---|---|---|---|---|---|---|---|---|
| ASTM B 348 [16] | Bal. | 5.5-6.75 | 3.5-4.5 | < 0.40 | < 0.08 | < 0.015 | < 0.05 | < 0.20 |
| Fine powder | Bal. | 6.08 | 3.88 | 0.19 | 0.02 | 0.005 | 0.02 | 0.17 |
| Coarse powder | Bal. | 6.02 | 3.92 | 0.22 | 0.03 | 0.006 | 0.02 | 0.17 |

*2.2 Laser-beam powder bed fusion*

To develop a processing map for the HDH Ti-6Al-4V powder with the two size distributions, different combinations of laser power (P), scan speed (or velocity, V), and hatch spacing (H) were selected (see Figure 2a). Fifty-three combinations of *P-V-H* were chosen to manufacture coupons of 15 × 10 × 10 $mm^3$ using an EOS M290 machine from the fine and coarse HDH Ti-6Al-4V powders. The layer thickness was constant at 60 µm (see ref. [17] for the reason of thickness selection). For each combination, two samples were LB-PBF processed to evaluate the printability of HDH powders. Figure 2b shows the layout of all as-built coupons fabricated on the base plate, and parts were removed using wire electrical discharge machining (GF Machining Solutions AC Progress VP3 Wire EDM Machine).

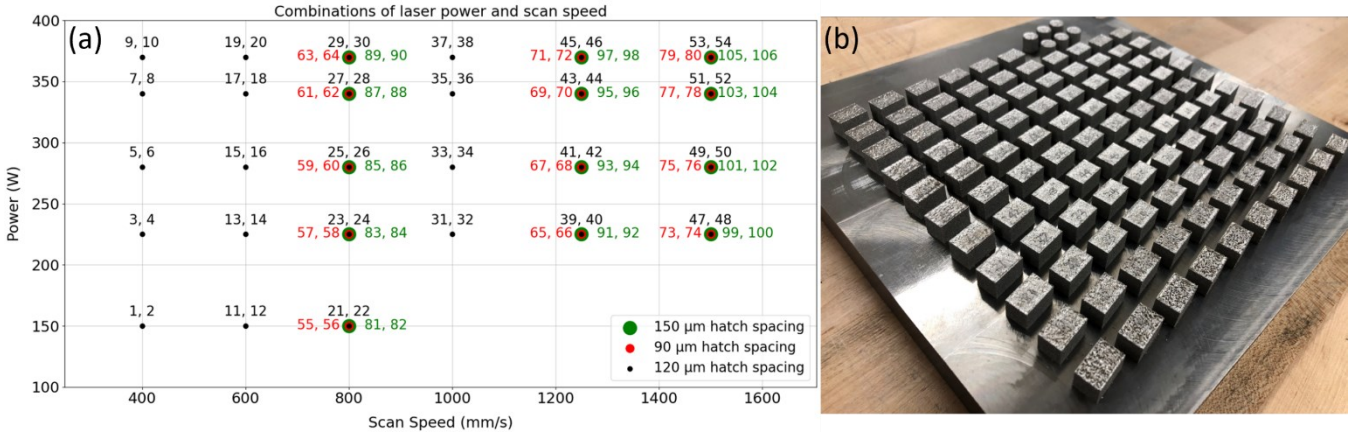


Figure 2. (a) An overview indicating process parameter combinations associated with sample numbers in which two coupons were LB-PBF processed for each *P-V-H* combination. (b) Photograph of the LB-PBF processed HDH Ti-6Al-4V parts to optimize process parameters of laser power, scan speed, and hatch spacing using the HDH powders.

*2.3 Characterizations of as-build coupons*

The relative density of the as-built coupons was measured using the Archimedes method to evaluate the density of the replicated coupons, and it was found that the standard deviation (std) was between 0.002-0.5. Smaller std values were attained for samples with relative densities of > 99.9 %. As-built samples were cross-sectioned parallel to the build direction using an EDM machine (Mitsubishi FX10k Wire EDM Machine) and mounted by fast cure acrylic powder resin and hardener (MetLab) for metallographic observations. Then, mounted samples were ground using sandpapers up to 800 grit sizes and polished using 3 µm diamond solution, 1 µm, and 0.05 µm alumina solution, then, samples were etched using Kroll's reagent. A Nikon Eclipse MA200 optical microscope was utilized to analyze the porosity. Optical images were taken from the entire vertical cross-section of sample surfaces at a magnification of 50× with a resolution of 1280×960 pixels and then were stitched, converted to binary with the suitable threshold, and analyzed using ImageJ software [18] to determine the percentage and size distribution of pores. The Vickers microhardness was measured on the vertical cross-section of the LB-PBF Ti-6Al-4V parts (fine powder) using a Buehler Micromet 2 machine with a load of 500 g and a dwell time of 15 s. Ten indentations were conducted on each sample, and the average number was reported.

*2.4 High-speed synchrotron x-ray imaging*

The dynamic x-ray radiography (DXR) experiments were performed at the 32-ID-B beamline of the Advanced Photon Source at Argonne National Lab. To replicate the laser melting conditions of the LB-PBF process, a miniature single-bead powder bed was set up in an argon

(1 atm) chamber where a ytterbium fiber laser with a wavelength of 1070 nm, maximum output power of 540 W, and spot size of 71.5 μm scans from the top. The powder bed consists of a powder layer (~ 200 μm) and a thin slab (1 mm thickness × 2.89 mm height) of Ti-6Al-4V substrate. The powder layer was placed on the top surface of the substrate which was sandwiched by two glassy carbon plates (1 mm thickness x 3 mm height). Polychromatic x-rays with the first harmonic energy of 24.4 keV were used to illuminate the powder bed. The transmitted x-rays were converted into visible light by a LuAG:Ce scintillator and later captured by a Photron FastCam SA-Z high-speed camera at a frame rate of 25,000 Hz.

*2.5 Powder packing analysis*

The powder packing analysis utilized the 2D vertical cross-sections of the powder computed tomography (CT) shown in Figure 3a as the input. The CT dataset was acquired in a Zeiss Metrotom 800 system using x-rays with 85 kV and 47 mA resulting in a spatial resolution of 5.4 μm/pixel. The powder specimen was contained in a Kapton tube with an inner diameter of approximately 3.49 mm. Figure 3b shows an example of a synthetic powder bed image consisting of a 120 μm powder layer, which was extracted from the powder tomography, and a solid substrate, which was assumed to be fully dense and possessed a smooth top surface. The selection of the 120 μm powder layer thickness was based on the 60 μm layer thickness used in the actual LB-PBF fabrication. As discussed in many studies [19,20] the powder layer thickness converges to a value, which can be approximated by $(\frac{layer\ thickness}{powder\ packing\ fraction})$, after the first ten layers of deposition. Semi-circular melt pools with various depths, from 43.2 μm to 411.2 μm with an increment of 21.6 μm, were overlaid on the powder bed image where only the overlapping area was used in the packing fraction calculation, i.e., the ratio between the black solid pixel and the white empty pixel, as shown in Figure 3b. Once the packing calculations at all melt pool sizes were completed, the model repeats the same process on a new powder bed image. A total of 660 images were used in this study.

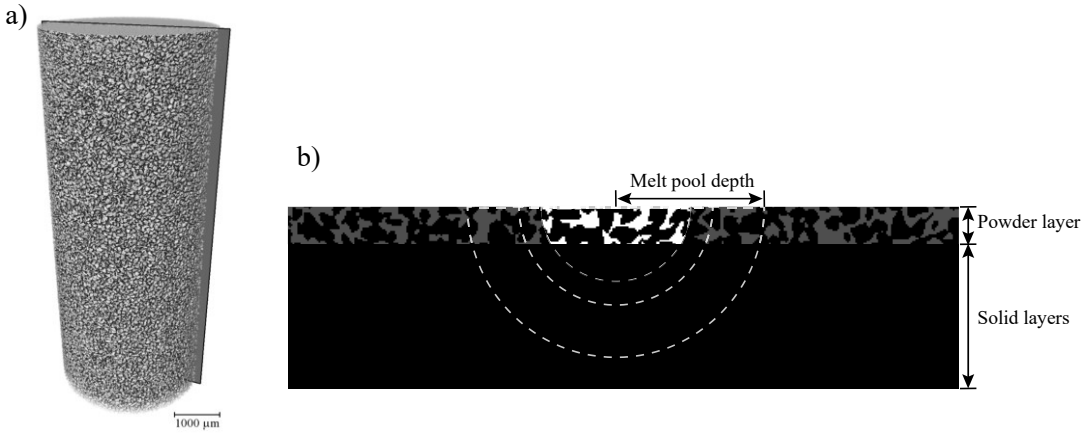


Figure 3. CT of the fine HDH powder with a cross-sectional plane demonstrating how the powder images were extracted in (a) and (b) an example synthetic powder bed image with semi-circular melt pools showing how the powder packing fraction was calculated.

## 3. Results and Discussion

*3.1 Powder flowability*

Flowability is an important indicator of powder's spreadability and printability, which is essential to the quality of powder bed in additive manufacturing. With the irregular shape, HDH

powder is expected to have lower flowability than GA powder owing to powder interlocking during spreading. It is shown in [8] that the GA powder had BFE and SE values of 365 mJ and 2.32 mJ/g, respectively, whereas for the HDH powder, they were 319 mJ and 2.40 mJ/g in coarse powder and 341 mJ and 2.7 mJ/g in fine powder, respectively. Surprisingly, the used HDH powders with the powder size distributions of 50-120 μm and 75-175 μm had even better flowability than GA powder with a powder size distribution of 20-63 μm. This better powder flow of the HDH powder is most likely because coarse powders are known to flow better than fine ones. The good flowability enables us to spread and form a high-quality HDH powder bed during LB-PBF to fabricate nearly fully dense components.

*3.2 Powder packing analysis using powder tomography*

Average packing fraction is the popular metric for quantifying powder packing; however, it overlooks the importance of local packing since pore formation is also a local event during laser melting. As proposed in our previous study [17], the local low-density packing spots could be the reason for the formation of pores akin to lack-of-fusion. They could result in depressions on the top surface of a melt track which later cause variation of layer thickness at the subsequent deposition and induce pore formation. The packing analysis was motivated by studies [21,22] from the geomechanics community where the concept of local packing was used to quantify the packing of porous media. The goal was to show if the powder size distribution and morphology could influence the local packing condition by comparing the fine HDH powder against the coarse HDH powder and the standard gas atomized powder reported in our previous study [17]. Although the powder specimen in a Kapton tube may not perfectly replicate an actual powder bed, the results do provide information about the relative packing of different powders.

Figure 4 summarizes the packing for each melt pool size into a single box-and-whisker plot highlighting the median, the $25^{th}$ and $75^{th}$ percentiles, and the minimum and maximum without considering the outliers. A smaller melt pool is more sensitive to the packing condition as suggested by the larger packing variation since the gas pockets between particles can easily dominate the area fraction of a melt pool when no solid substrate is re-melted. As the melt pool size increases, the variation of packing fraction significantly decreases as more remelting occurs with a bigger melt pool. Since the solid substrate was set to be fully dense, remelting also shifted the medians upward and away from the average packing fraction at larger melt pool depths as shown in Fig4. This observation aligns well with our optimization strategy in the fabrication which is to promote pore escape by increasing energy density. The average packing is 54.76% in the fine HDH powder specimen which is similar to the 53.93% and 58.02% average packing in the coarse HDH powder and the standard gas atomized powder [17], respectively. However, when only focusing on the common size range of LB-PBF melt pools (highlighted in green in Figure 4), the fine HDH powder specimen obviously possessed many low packing density spots with as low as 20% packing fraction. By contrast, the standard powder maintains a minimum packing of 50% for the same melt pool size [17]. Furthermore, the difference in powder packing density between the coarse and fine HDH powders was insignificant. Similarly, the porosity results discussed in the later section also show that limited options of laser power and speed combination are available for fabricating components with >99.9% density when using the fine HDH powder. That said, in addition to size distribution, powder morphology is another important factor affecting packing. Yet, further optimization is possible if more fine powder is added to reduce local packing variation by filling interparticle air pockets.

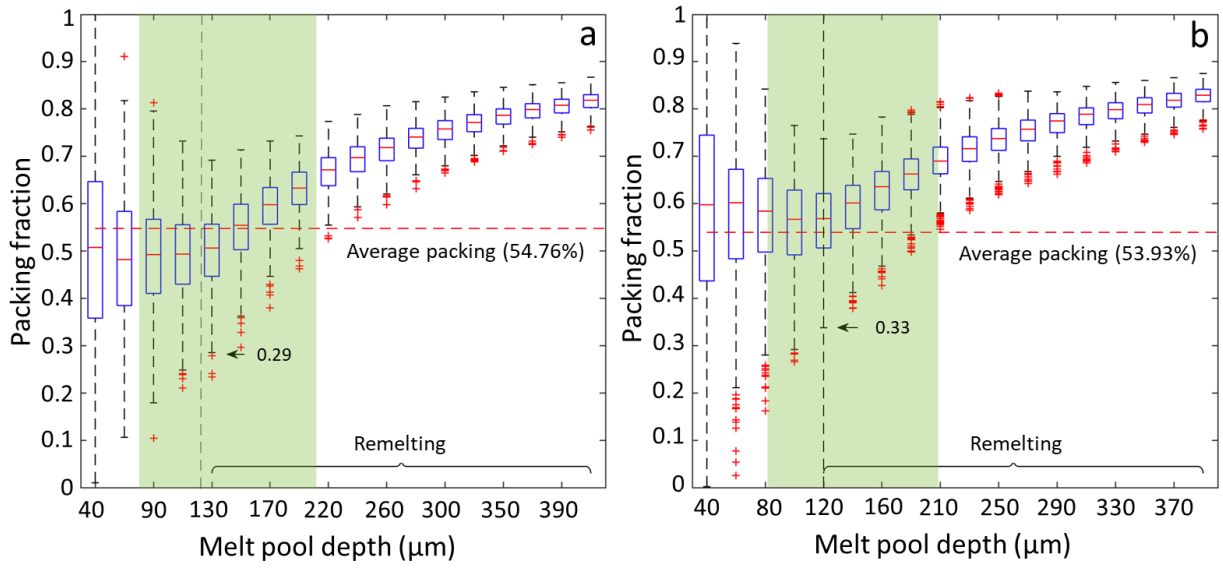


Figure 4. Powder packing fractions at various melt pool sizes in a) a fine HDH Ti-6Al-4V powder specimen and b) a coarse HDH Ti-6Al-4V powder specimen (reprinted from [17]). Note that the average packing was calculated using only the powder µXCT images; thus, there is a difference between the median of packing at a specific melt pool depth and the average packing, especially when remelting occurred.

### *3.3 Density measurements and porosity analysis of LB-PBF processed HDH Ti-6Al-4V*

The relative densities of LB-PBF processed HDH Ti-6Al-4V from both fine and coarse powders were measured based on image analysis on the cross-section of as-build coupons, and results were shown in Figure 5. The process map was optimized by means of adjusting the laser power, scan speed, and hatch spacing in the range of 150-370 W, 400-1500 mm/s, and 90-150 µm, respectively. In critical components for aerospace application, full density, defect-free AM parts are needed (e.g., a relative density of ≥ 99.9%) [23]; while in our study, we consider a relative density of >99.5% as part of the process map, and further tuning of process parameters can be applied to expand the process window such that higher densities can be attained. Figure 5 illustrated three main regions of (1) green – parts with lack of fusion porosity (LoF), (2) purple – parts with keyhole porosity, and (3) white – parts with a relative density of >99.5%.

Typically, large, irregularly shaped pores are categorized as LoF porosity, which is severely detrimental to ductility and fatigue resistance [24], and they often contain unmelted powder particles. LoF defects form in the LB-PBF processed parts due to inadequate melt pool overlap [25] as well as powder characteristics (i.e., here, non-spherical powder of HDH Ti-6Al-4V), laser beam fluctuations, and gas flow, leading to imperfect powder bed melt formation [25–28]. On the *P-V* map, LoF porosity occupies the low laser power and high scan speed regions. In past years, energy density has been used as a measure to predict the relative density of AM parts; however, it is possible for similar energy densities to result in different final densities (varying by as much as 60%) [29].

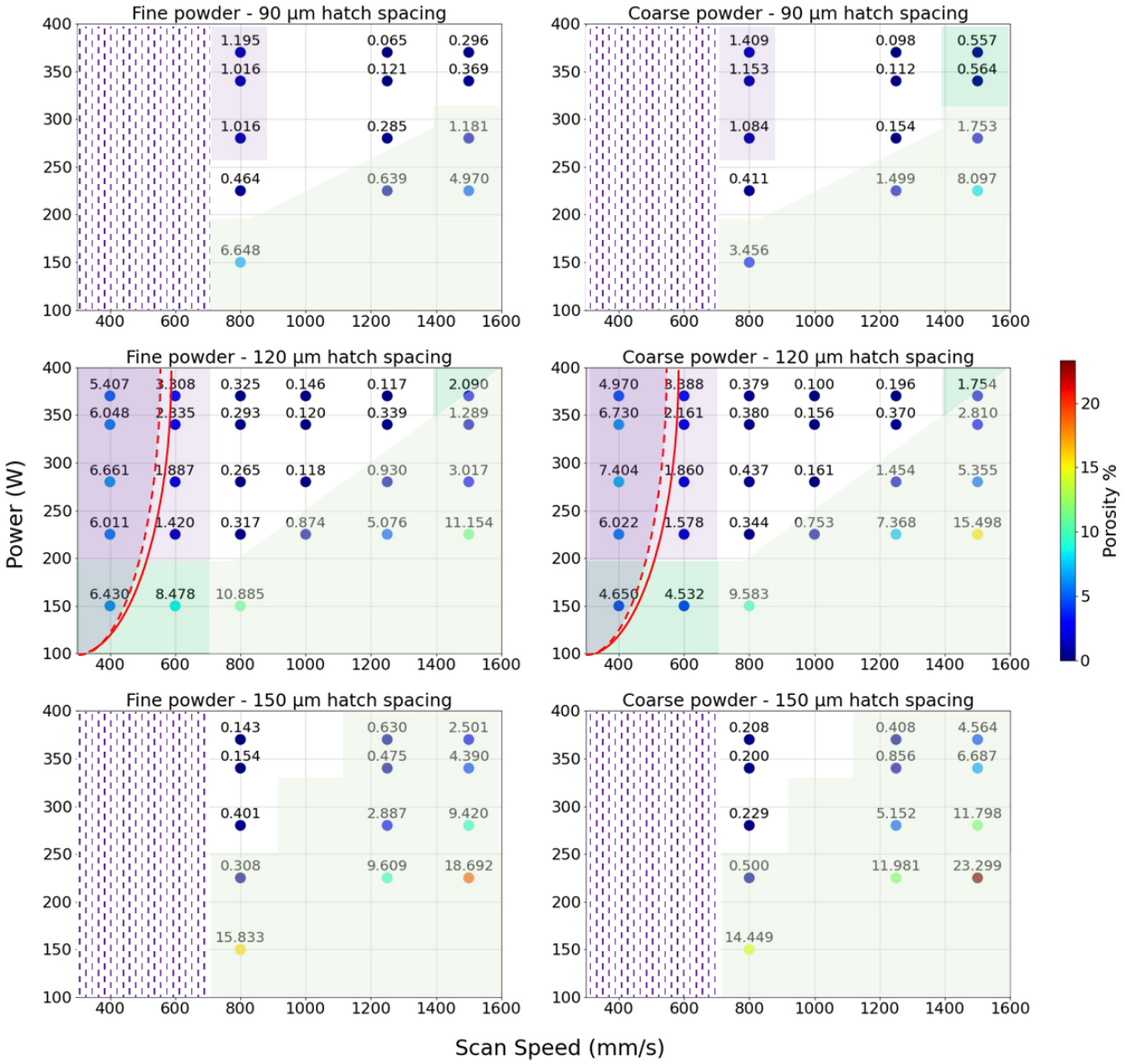


Figure 5. Porosity percentage of the LB-PBF processed HDH Ti-6Al-4V powder using different combinations of printing parameters of laser power, scan speed, and hatch spacing. The purple region indicates keyhole porosity, and the green regions denote lack of fusion porosity areas. The process window (white area) is defined as the area with a relative density >99.5%. In the middle row, the curved lines indicate the boundary between the keyhole porosity regime on the left and the stable melting regime on the right (consisting of a stable keyhole, transition, and conduction regimes). The Red dashed line shows the boundary for the bare plate and the red solid line shows the boundary when the powder is deposited on the plate [30].

Tang et al. [25] developed a simple geometric model to predict the boundary of the LoF porosity for Ti-6Al-4V, called LoF index, as follow:

$$\left(\frac{H}{W}\right)^2 + \left(\frac{L}{D}\right)^2 \leq 1 \qquad \text{(Eq. 1)}$$

where $H$ is the hatch spacing, $W$ is the melt pool width, $L$ is the layer thickness, and $D$ is the melt pool depth. This model assumes that a melt pool with semi-circle geometry forms such that melt pool width ($W$) is twice the melt pool depth ($D$), i.e., $W = 2D$. Therefore, we can differentiate the Rosenthal equation [31] and approximately calculate the melt pool depth as follow:

$$D = \sqrt{\frac{2Q\varepsilon}{\pi e \rho C_p V (T_m - T_0)}} \quad \text{(Eq. 2)}$$

where $Q$ is the laser power, ε is the absorptivity of Ti-6Al-4V alloy, $e$ is the base of natural logarithms, $\rho$ is the density of the bulk Ti-6Al-4V alloy, $C_p$ is the specific heat capacity of the bulk Ti-6Al-4V, $V$ is the scan speed, $T_m$ is the melting temperature, and $T_0$ is the pre-heat temperature such that ($T_m$ - $T_0$) (see Table 2).

Table 2. Physical properties of Ti-6Al-4V alloy [4,32].

| **Physical Property** | **Sign** | **Value** |
|---|---|---|
| Absorptivity | ε | 0.48 |
| Bulk density *[kg/m$^3$]* | $\rho$ | 4430 |
| Specific heat capacity *[J/kg.K]* | $C_p$ | 526 |
| Melting temperature *[K]* | $T_m$ | 1660 |
| Thermal conductivity *[W/m.K]* | $k$ | 6.7 |
| Thermal diffusivity *[m$^2$/s]* | $\alpha$ | $2.87\times10^{-6}$ |

The melt pool depth and melt pool width were estimated using Eq. 2, and results were shown in Figure 6. The LoF boundary was determined based on Eq. 1, and values higher than 1 were considered improper *P-V-H* combinations resulting in large, irregular pores, in agreement with 2D micrograph analyses on the cross-section of the as-build specimens (green areas in Figure 5). Two regions in Figure 6 are (1) values higher than 1 in which LoF porosity is expected and (2) values much less than 1 in which the geometric model predicts the reduced occurrence of LoF porosity. In other words, it can be assumed that the content of irregular defects decreases when the LoF index values decrease. For instance, samples #99 (fine powder) and #100 (coarse powder) had an LoF index of about 2.05 which was over 100% higher than 1; therefore, it was assumed that most pores were LoF porosity due to a consequence of insufficient melt pool overlap. Green dash lines in Figure 6 represent a nominal build rate of 4.5 mm$^3$/s derived from nominal printing parameters (see Table 3) provided by the EOS M290 manufacturer to obtain an optimum relative density of 99.5%.

One may use $\frac{H}{W}$ and $\frac{L}{D}$ ratios to characterize melt pool overlap. When $\frac{L}{D}$ ratio is less than 1, sufficient vertical overlap is achieved and LoF is lowered. Also, lateral overlap or $\frac{H}{W}$ should remain below 1 to minimize sensitivity to process settings [25]. Those *P-V-H* combinations with reduced $\frac{H}{W}$ and $\frac{L}{D}$ ratios indicated sufficient melt pool overlap and lowered chance of LoF porosity. As an example, specimens #71 (*P*: 370 W, *V*: 1250 mm/s, and *H*: 90 µm with a relative density of 99.935%) and #72 (*P*: 370 W, *V*: 1250 mm/s, and *H*: 90 µm with a relative density of 99.902%) had an LoF index of 0.634 and $\frac{H}{W}$ and $\frac{L}{D}$ ratios of 0.478 and 0.637, respectively. In the *P-V* maps with the hatch spacing of 120 µm (in both fine and coarse powders), there were three combinations of 150 W & 400 mm/s (Samples #1 and #2), 150 W & 600 mm/s (Samples #11 and #12), and 370 W &1500 mm/s (Samples #53 and #54) with LoF index of 0.641, 0.961, 0.974, respectively, in which LoF porosity was seen on micrographs (see Figure 7). This could be attributed to the low powder packing density of HDH powder and low laser power of 150 W (leading to the formation of a shallow melt pool) or capillary instability of the melt pool due to high laser power and high scan speed.

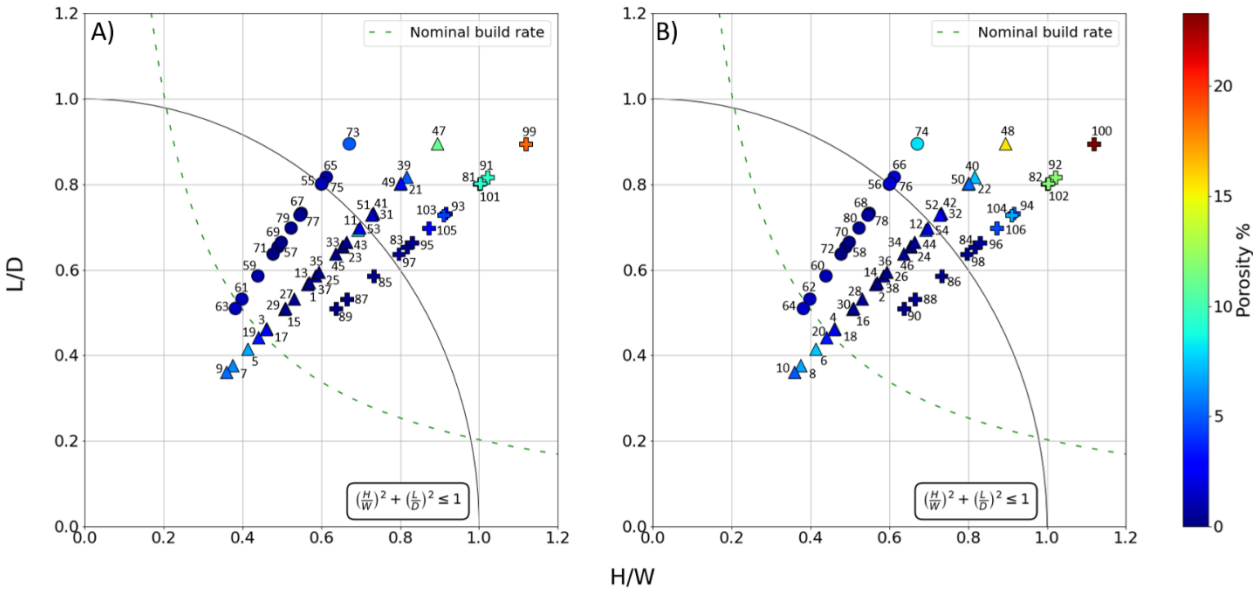


Figure 6. Processing map of hatch spacing and layer thickness relative to melt-pool dimensions of melt pool depth and width of samples fabricated using A) fine and B) coarse powder; conditions within the circular arc would avoid irregular lack-of-fusion porosity (LoF index) which means melt pool overlap and overlap depth must obey geometric criterion.

In addition to irregular pores, spherical keyhole porosity may be generated in the LB-PBF process powder during keyhole printing mode [30,33]. Formation of this defect usually occurs at low scan speed and high laser power. At a high laser power, the laser drills deeper into the base plate forming a "J" shaped melt pool (elongated melt pool) with a vapor cavity in the center. In other words, keyholes with a high depth-to-width ratio show a strong tendency for pinching off the tip of the keyhole. Recently, Zhao et al. [30] revealed that the boundary between the keyhole porosity and stable melting regimes in the *P-V* process map of spherical Ti-6Al-4V powder has a non-linear relationship with laser power and scan speed, as indicated by two curved lines in Figure 5. It is worth noting that the keyhole porosity (shape and size) is affected by keyhole depth during keyhole printing mode. The determined unstable keyhole porosity regime (left side of the red dashed line) resulted in a large keyhole pore formation. For instance, at a constant scan speed of 400 mm/s, it was seen when the laser power increased from 150 W (Sample #1) to 370 W (Sample #9), variation in porosity percentage was minimal but microscopy observation and pore analysis revealed evolution in pore morphology and size distribution (see Figure 7 and Figure 8). In fact, LoF pores were dominant defect in the microstructure when low laser power of 150 W was applied then by increasing it to 225 W, a transition from the conduction to keyhole mode resulted in the formation of round keyhole pores (due to entering to the unstable regime at low scan speed of 400 mm/s and gas bubble entrapment inside the melt pool occurred). The right side of the boundary (see the red curved line in Figure 5) (stable melting regime) consists of stable keyhole, transition, and conduction regimes. In another situation in which the power was constant (e.g., 340 W), keyhole pores appeared in the microstructure (due to unstable key mode printing) when the scan speed was ≤ 600 mm/s; while a transition between non-stable to stable keyhole mode (e.g., at laser scan speed of > 600 mm/s) resulted in the formation of minimal spherical pores in the process window with less than 0.5% pores in the microstructure. As the scan speed was set at 1500 mm/s, a transition from keyhole to conduction mode led to the formation of LoF pores.

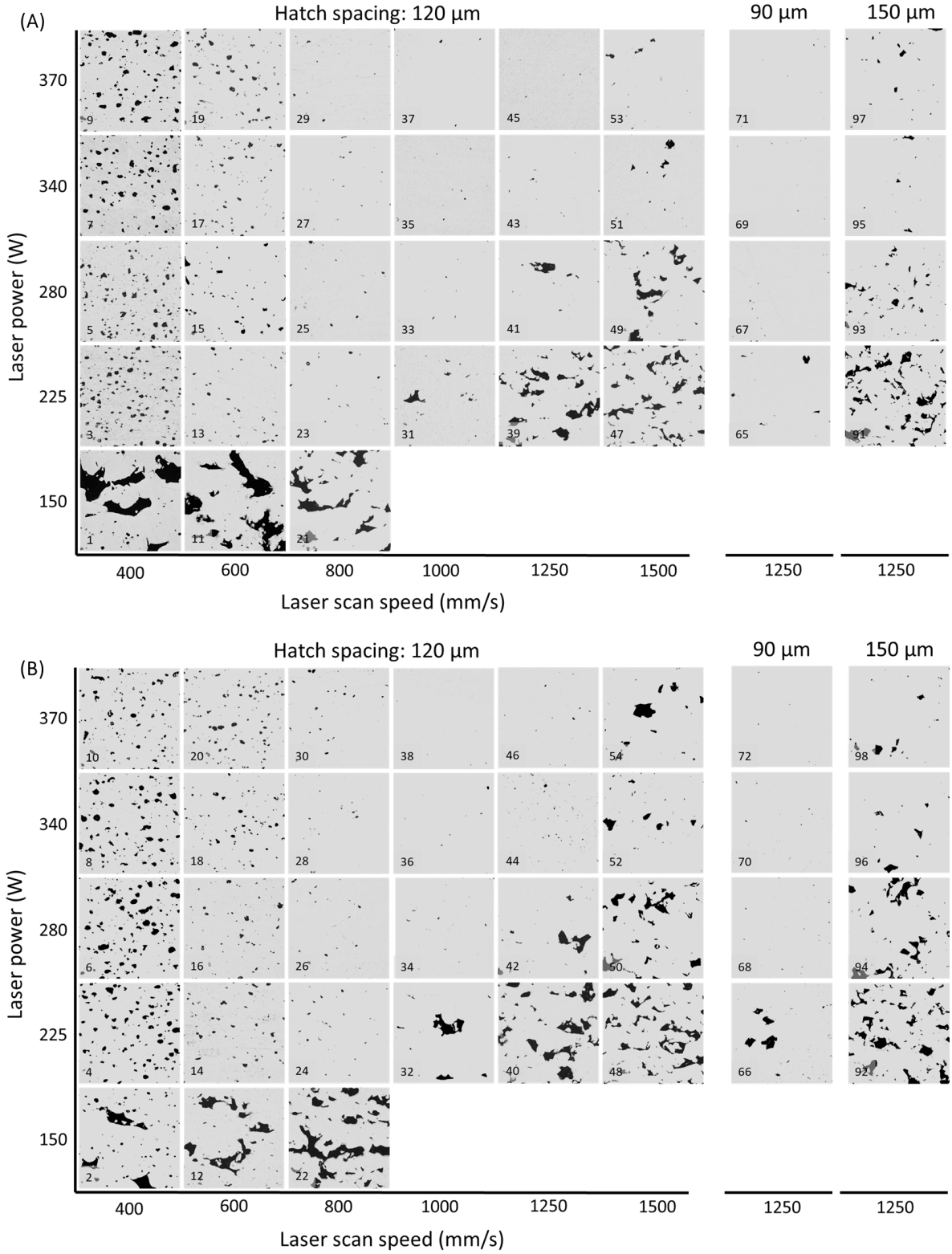


Figure 7. Optical micrographs taken from cross-section of the LB-PBF processed HDH Ti-6Al-4V (A) fine and (B) coarse feedstock using different laser power-scan speed-hatch spacing combinations. Numbers represent sample numbers and odd numbers in "A" represent LB-PBF of fine powder and even numbers in "B" represent LB-PBF of coarse powder. Irregular coarse pores are known as lack-of-fusion porosity, which can be interconnected, while fine isolated pores are known as keyhole pores. In some cases, fine circular pores in 2D micrographs might be evolved due to improper powder pack density of the HDH powder.

In Figure 5 and for the hatch spacing of 120 µm, the area between the dashed and solid lines indicated the difference between presence and absence of powder during the laser melting process, the deposition of powder expanded the keyhole porosity regime to higher scan velocities at a constant power; nevertheless, the expansion seemed inadequate to explain remnant porosities in the LB-PBF processed HDH Ti-6Al-4V powder. Thus, the proposed keyholing boundary (at the presence of metal powder) in [30] would be shifted to the right side when non-spherical powder is used, perhaps because of stronger interruptions of the laser beam by the non-spherical powder surfaces. This matter can be evaluated by synchrotron x-ray high-speed imaging in which the laser-powder interactions can be visualized *in-situ*. Finally, *P-V-H* combinations indicated that, when the hatch spacing decreased from 120 µm to 90 µm, the process window expanded slightly, however, increasing the hatch spacing from 120 µm to 150 µm resulted in a smaller process window that was shifted to slower scan speeds.

Figure 8 shows cumulative pore size distributions on a probability scale (Figure 8a,b) and normalized pore size distributions from the 2D micrographs (Figure 8c,d). Data was collected from the cross-sectional optical micrographs of the specimens shown in Supplementary Figure 1. By comparing pore distributions of sample #45 ($H$: 120 µm and density of 99.883%) with sample #71 ($H$: 90 µm and density of 99.935%), along with increasing hatch spacing from 90 to 120 µm, the size distribution of porosities is significantly changed such that the porosity size distribution is broader in sample #45 compared to sample #71. Additionally, the maximum size of pores in sample #45 is higher than sample #71 by about 50 µm (see Figure 7 and Figure 8c). This difference in pore size distribution can be explained by the difference in melt pool lateral overlap ($\frac{H}{W}$) of these two fabricated parts (see Figure 6). Sample #71 with $\frac{H}{W}$ of 0.477 has higher melt pool lateral overlap than sample #45 with $\frac{H}{W}$ of 0.637. This higher lateral overlap resulted in better remelting of the previously solidified melt pool, thus, removing the majority of bigger porosities [25]. The explained point was observed during comparison of samples #1, #2 ($P$: 150 W, $V$: 400 mm/s, $H$: 120 µm, $\frac{H}{W}$: 0.566), #21 and #22 ($P$: 150 W, $V$: 800 mm/s, $H$: 120 µm, $\frac{H}{W}$: 0.8) with samples #9, #10 ($P$: 370 W, $V$: 400 mm/s, $H$: 120 µm, $\frac{H}{W}$: 0.36), #89 and #90 ($P$: 370 W, $V$: 800 mm/s, $H$: 150 µm, $\frac{H}{W}$: 0.637), respectively (see Figure 6).

By comparing sample #1 ($P$: 150 W and $V$: 400 mm/s) and sample #21 ($P$: 150 W and $V$: 800 mm/s), it was seen that (i) porosity characteristics moved from below LoF criterion to over LoF criterion (see Figure 6a) and porosities were transformed from keyhole mode to LoF along with an increase in total porosity percentage by about 4.4%, (ii) probability of having porosities with an effective diameter of < 25 µm increased, however, probability of having porosities with an effective diameter of > 25 µm decreased (Figure 8a), and (iii) maximum size of porosity decreased by 120 µm from 620 µm to 500 µm (Figure 8c). Furthermore, Figure 7 also confirmed that there were many small keyhole pores and a small number of large LoF pores in sample #1, which could be related to the lower packing density and larger packing variation of non-spherical powder compared to standard gas atomized powder. On the other hand, sample #21 showed fewer keyhole pores and more LoF pores than sample #1, which confirmed (i) and (ii).

To investigate the effect of laser power on porosity evolution, samples #2 ($P$: 150 W) and #10 ($P$: 370 W) with the same scan speed of 400 mm/s were selected. Sample #2 showed a density of 95.35% and sample #10 had a density of 95.03%, which is not so much different. Both samples show similar porosity size probability distribution, but sample #2 had the maximum porosity

effective diameter of 431 µm, while, sample #10 had the maximum porosity effective diameter of 185 µm (see Figure 7B and Figure 8b,d). With increasing laser power from 150 W to 370 W, the total number of porosities decreased from 66 to 44 per $mm^2$ and porosities became substantially smaller without any significant changes in the total density of parts. Therefore, probability plots for the distribution of porosity and distribution of the residual pores vs. effective diameter provided valuable information on the porosity characteristics such as size, number, and distribution as a function of laser power, scan speed, and hatch spacing. We found that (i) higher scan speed and higher laser power further reduce the porosity population, (ii) reducing hatch spacing further improves the part density, (iii) pores smaller than 30 µm dominates the porosity population if the parameter is within the process map, (iv) high scan speed and low laser power lead to the LoF pore formation in which large and interconnected pores dominate the pore volume, and (v) the LoF pores align along the scanning direction.

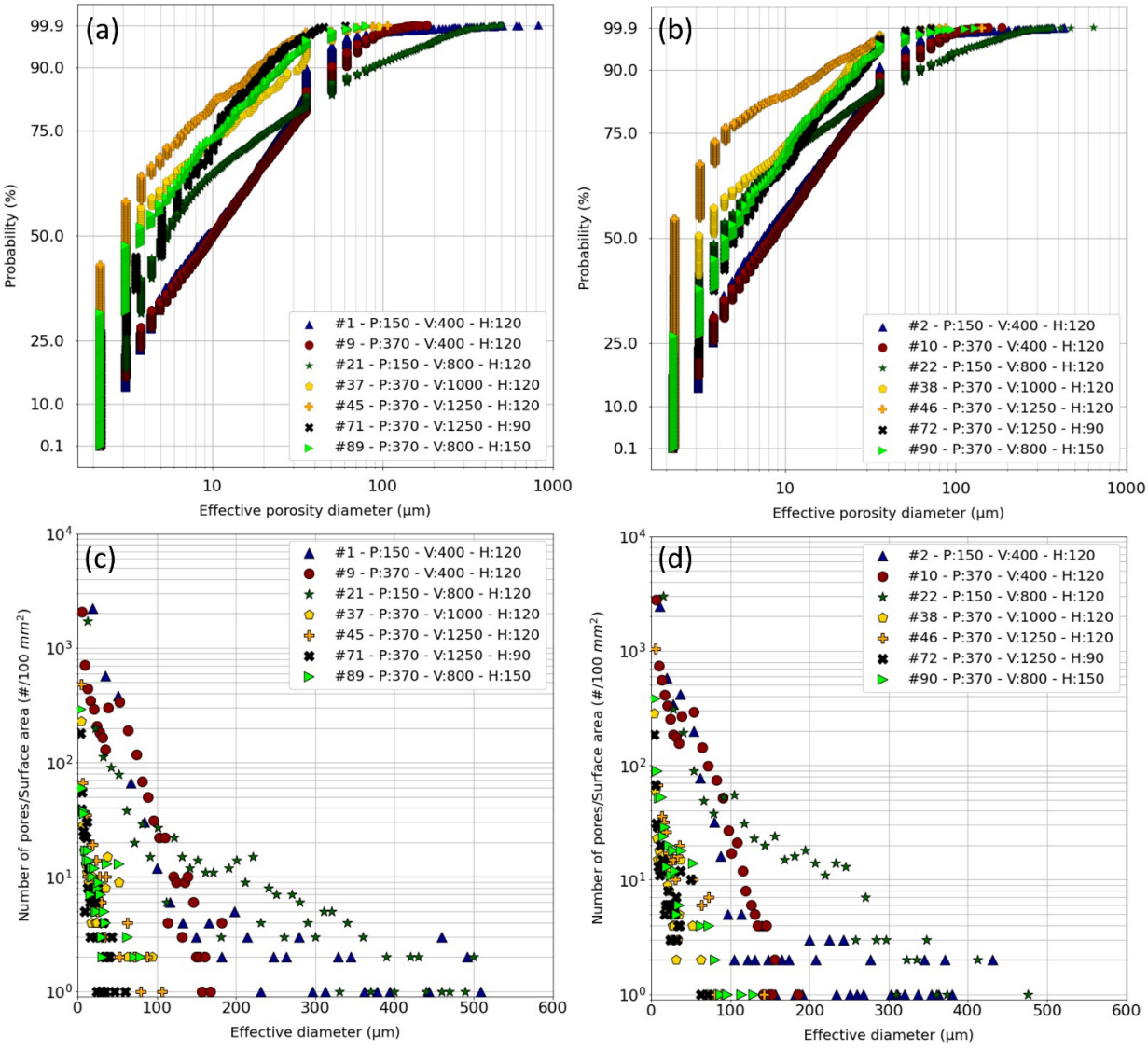


Figure 8. A comparison of probability plots indicating the cumulative porosity size distributions of the LB-PBF processed (a) fine and (b) coarse HDH Ti-6Al-4V powders. Distribution of the residual pores vs. effective diameter on the entire cross-section for the LB-PBF processed (c) fine and d) coarse HDH Ti-6Al-4V powders.

### *3.4 Energy density vs. density of LB-PBF processed HDH Ti-6Al-4V*

The relative density of samples against energy density was shown in Figure 9. The volumetric energy density (as opposed to linear energy density) is a parameter used to describe the average input energy on material per volume [34] as follow:

$$E = \frac{P}{V.H.L} \quad \text{(Eq. 3)}$$

where $P$ is laser power (J), $V$ is laser scan speed (mm/s), $H$ is hatch spacing (mm), and $L$ is layer thickness (mm). As shown in Figure 9a, there is a general trend of achieving higher densities of >99.5% with some outliers that can be explained by the individual effects of printing parameters. When laser power and scan speed are doubled, the energy density would remain constant at constant hatch spacing and layer thickness. However, changes in laser power and scan speed directly affect melt pool geometry and the ability of the laser to melt the powder throughout the volume. Thus, the final density of parts would be affected.

Figure 9b showed the effect of melt pool geometry on porosity difference between parts manufactured using the same printing parameters but different powders (fine and coarse) with respect to the parameters used for the printing, which were shown as energy density (Eq. 3). Melt pool geometry is shown by the ratio of $\frac{L}{W}$ derived from the Rosenthal equation and described as follows [31]:

$$\frac{L}{W} = \sqrt{\frac{\varepsilon e Q V}{32\pi k \alpha (T_m - T_0)}} \quad \text{(Eq. 4)}$$

where $L$ is melt pool length, $W$ is melt pool width, $Q$ is laser power, $V$ is laser scan speed, $e$ is the base of the natural logarithm, $\varepsilon$ is laser absorptivity of Ti-6Al-4V alloy, $k$ is the thermal conductivity of Ti-6Al-4V, $\alpha$ is the thermal diffusivity of Ti-6Al-4V, $T_m$ is the melting temperature, and $T_0$ is the pre-heat temperature such that ($T_m$ - $T_0$) (see Table 2).

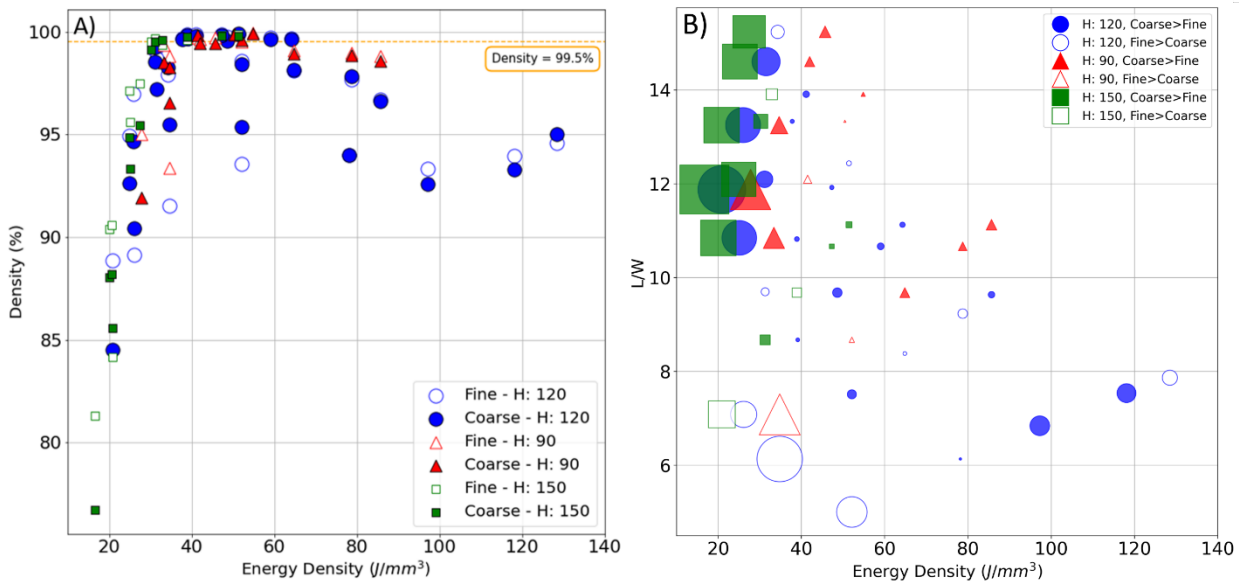


Figure 9. (A) Relative density of LB-PBF HDH Ti-6Al-4V parts fabricated with the corresponding energy density and (B) the relationship between melt pool geometry (y-axis), energy density (x-axis), and the porosity difference between samples printed with fine and coarse powders (size of points). The orange dashed line in (A) denotes the density of 99.5% threshold to find the proper energy density for printing parts. Solid shapes in (B) denote the higher porosity percentage of samples manufactured using coarse powder and hollow shapes denote the higher porosity percentage of

samples manufactured using fine powder. Size of the shapes in (B) shows the magnitude of porosity content difference between coarse and fine powder.

The general trend showed higher sensitivity to powder feedstock as the energy density is below 40 J/mm$^3$. It was seen that with decreasing energy density, porosity difference tends to increase. On the other hand, for $\frac{L}{W}$ of lower than 10, the fine powder shows more porosity content than the coarse powder, and this difference decreases by increasing the $\frac{L}{W}$ up to 10. By increasing $\frac{L}{W}$ up to 12, the porosity content in coarse powder increases, and for $\frac{L}{W}$ of higher than 12, the porosity difference tends to decrease (see Figure 9b). These variations in porosity content can occur due to the more severe shadowing (see section 3.7) effect in coarse powder. When the laser scan speed is larger (e.g., L/W ratio higher than 10), laser moves on the particles faster and the shadowing effect prevents full remelting of the previous layers because of high keyhole depth fluctuations, thus, a higher amount of porosity will prevail. On the other hand, when the powder size is smaller (i.e., using fine HDH powder), the shadowing effect will be of less importance; however, smaller powder size resulted in a higher number of powder particles in the same volume which led to a less remelting rate of the previously deposited layer using low laser power and scan speed (e.g., L/W ratio lower than 10). The smaller remelting rate caused a higher porosity percentage in the samples manufactured using fine powder. When the energy density is above 40 J/mm$^3$, sensitivity to powder feedstock decreases. This suggests that the shape of the melt pool (e.g., depth and width) may play an essential role in how easily pores escape from the melt pool. Although powder packing density of both fine and coarse powder is about 54%, fine powder showed more low packing spots compared to coarse powder (see Figure 4) which can lead to void formation during the powder spreading. This would impact melt pool formation when the energy density is < 40 J/mm$^3$. Since powder packing density of the irregularly shaped powder is lower than the spherical ones (54% compared with 58%), it is thought that the energy density higher than 40 J/mm$^3$ will generate a sufficiently deeper melt pool (in transition or stable keyhole mode printing) compared to the conduction mode printing with a shallower melt pool, and therefore may facilitate pore escape.

*3.5 Build rate vs. density of LB-PBF processed HDH Ti-6Al-4V*

In metal AM, quantitative prediction of near fully dense part production as a function of the build rate is crucial, specifically when non-standard powders are developed in powder bed AM machines. The proposed geometric model by Tang et al. [25] was developed with a particular aim to enhance the build rate. The following Eq. 5 can be used to calculate the build rate:

$$\text{Build rate} = V.H.L \qquad \text{(Eq. 5)}$$

where $V$ is the laser scan speed, $H$ is the hatch spacing, and $L$ is the layer thickness. In this study, the layer thickness was fixed at 60 μm, while both scan speed and hatch spacing were varied to improve build rate at which the density of > 99.5% was achievable, and the results of build rate ratio vs. density are shown in Figure 10. To maximize the build rate, a high scan speed is preferred, and a high laser power is required to enhance the melt pool depth and the remelting fraction of the previously deposited layer, while the *P-V* combination should be optimized to avoid balling. Further, the analytical Rosenthal equation for the melt-pool size (see Eq. 2) is proportional to the root square of $P/V$, thus, increasing the melt pool size at a constant power can be achieved by reducing scan speed. This will reduce the build rate, and if $V$ is below a certain speed (see the red dash line in Figure 5), keyholing porosity occurs.

One practical implication in Figure 10 is that in many cases, there is room to increase the build rate without causing LoF porosity. Typically, build rate ratios between 1.5 and 2 (absolute build rates of 6.75 and 9 $mm^3/s$) resulted in densities of > 99.5% and one can choose a variety of *P-V-H* combinations to manufacture near fully dense parts. It is worth noting that the energy density and build rate have an inverse relationship and it will directly affect the melt pool geometry and microstructure of the AM parts. Tang et al. [25] reported that the maximum build rate would be achieved at equal values of *H/W* and *L/D*, both equal to 0.71. However, this value was not seen in this study, and based on the hatch spacing, a variety of *H/W* and *L/D* combinations could lead to the fabrication of near full density AM parts. A summary of the process parameters, energy density, and build rate of selected LB-PBF samples that resulted in the fabrication of parts with densities of 99.8% was given in Table 3. Compared to the standard process parameter for spherical Ti-6Al-4V powder in the EOS M290 machine, higher build rates can be attained using non-spherical HDH Ti-6Al-4V powder with much larger particle sizes. One main difference was the layer thickness of 60 µm compared to 30 µm used for standard spherical powder (with $d_{50}$ = 39 µm). However, the larger layer thickness may cause some loss of geometrical resolution which illustrates the necessity to maximize build rate with all constraints taken into account.

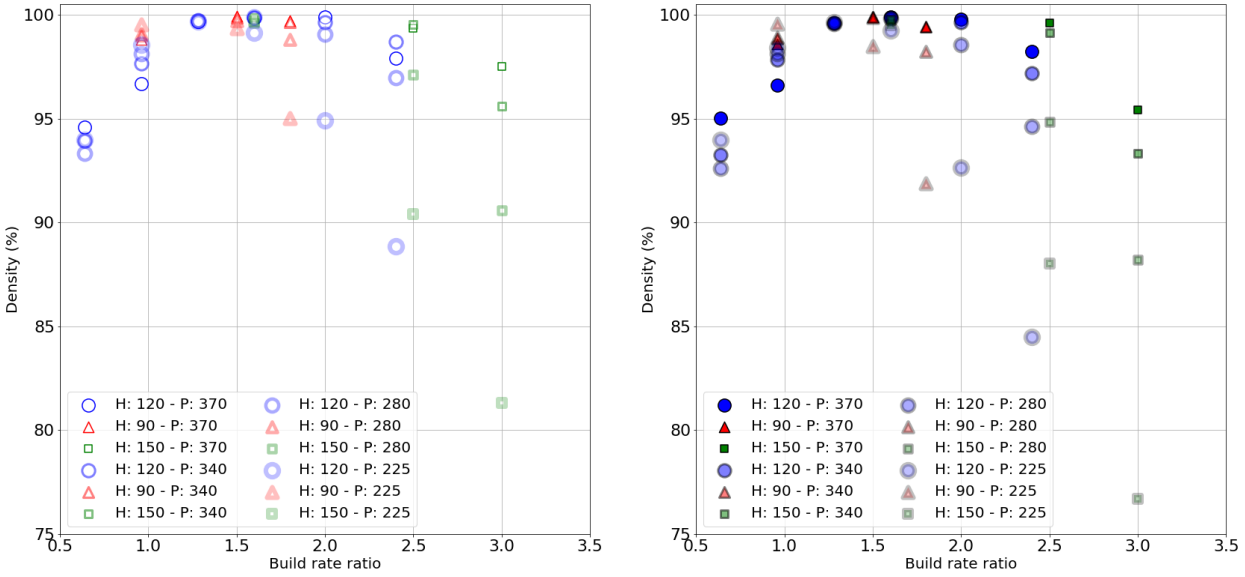


Figure 10. Density variation based on varying LB-PBF process parameters of the fabricated parts from HDH Ti-6Al-4V (left) fine and (right) coarse powders. The build rate ratio is the rate compared to the standard condition (power of 340 W, scan speed of 1250 mm/s, hatch spacing of 120 µm, and layer thickness of 30 µm). Build rate increases as the scan speed increases from 400 mm/s to 1500 mm/s.

Table 3. Summary of process parameters, build rate, and energy density of selected samples with a relative density of > 99.8 %. Nominal process parameters for LB-PBF of spherical Ti-6Al-4V were provided by the EOS M290 machine manufacturer. Note: The spherical powder used in the EOS M290 machine had $d_{50}$ = 39 µm, while HDH powder had a significantly higher median size, i.e., $d_{50}$ = 82 µm and $d_{50}$ = 109 µm for fine and coarse powders, respectively.

| Samples No. | P (W) | V (mm/s) | H (µm) | L (mm) | Build Rate ($mm^3/s$) | Energy Density ($J/mm^3$) | Relative Density (%) |
|---|---|---|---|---|---|---|---|
| 27 | 340 | 800 | 120 | 60 | 5.67 | 59 | 99.707 |
| 28 | 340 | 800 | 120 | 60 | 5.67 | 59 | 99.620 |
| 37 | 370 | 1000 | 120 | 60 | 7.2 | 51.4 | 99.854 |
| 38 | 370 | 1000 | 120 | 60 | 7.2 | 51.4 | 99.900 |
| 45 | 370 | 1250 | 120 | 60 | 9 | 41.1 | 99.883 |
| 46 | 370 | 1250 | 120 | 60 | 9 | 41.1 | 99.804 |

| | | | | | | | |
|---|---|---|---|---|---|---|---|
| 71 | 370 | 1250 | 90 | 60 | 6.75 | 54.8 | 99.935 |
| 72 | 370 | 1250 | 90 | 60 | 6.75 | 54.8 | 99.902 |
| 83 | 225 | 800 | 150 | 60 | 7.2 | 31.3 | 99.692 |
| 84 | 225 | 800 | 150 | 60 | 7.2 | 31.3 | 99.500 |
| 89 | 370 | 800 | 150 | 60 | 7.2 | 51.4 | 99.857 |
| 90 | 370 | 800 | 150 | 60 | 7.2 | 51.4 | 99.792 |
| Nominal | 340 | 1250 | 120 | 30 | 4.5 | 75.5 | 99.548 |

*3.6 Microstructure of LB-PBF processed HDH Ti-6Al-4V*

To observe the microstructure of the LB-PBF processed HDH Ti-6Al-4V, samples with a relative density of > 99.8% were selected. Figure 11 showed the optical micrographs taken from the center of the vertical cross-section of the etched samples. The vertical cross-sections clearly show an epitaxial growth (elongated columnar grains), as reported elsewhere [34–36]; The shape of the grains is sensitive to variations of melt pool geometry due to the different LB-PBF process parameters. Owing to the high cooling rates in LB-PBF, a fine acicular martensitic (α′) structure was seen in the elongated grains. Columnar prior β grains were present in all microstructures extending over multiple layers. The epitaxial growth resulted from the remelting and resolidification processes which allow the preferred orientation from the previous deposition to be inherited [37]. Depending on the process parameters (laser power, scan speed, and hatch spacing), the size of prior β grains varied from 0.10 mm to 0.20 mm in width and from 0.4 mm to 4 mm in length, confirming prior β grains were far taller than the layer thickness of 60 µm. At a constant laser power of 370 W, when the scan speed increased from 1000 mm/s (samples #37, #38) to 1250 mm/s (samples #45, #46), the energy density decreased from 51.4 J/mm$^3$ to 41.1 J/mm$^3$, indicating a reduction of heat input; thus, a smaller β grain width and shallower melt pools were seen. At the constant power of 370 W and scan speed of 1250 mm/s, when the hatch spacing decreased from 120 µm (samples #45, #46) to 90 µm (sample #71), the energy density increased from 41.1 J/mm$^3$ to 54.8 J/mm$^3$ leading to the formation of coarse β grains. It could be associated with the increase in overlap of the melt tracks and the resulting heat buildup influencing melt formation, solidification conditions, and consequently the resultant grain width [8]. At the highest energy density of 54.8 J/mm$^3$, it was observed that the thick and textured columnar grains, which span the entire specimen length, were formed; at a lower energy density of 41.1 J/mm$^3$, the columnar structure was possibly broken, resulting in a microstructure of the prior β grains. The above observations were consistent with enhanced epitaxial growth at high energy densities because of the directional thermal gradients and partial re-melting of previously deposited layers as reported in [38].

The microstructures of the various LB-PBF HDH Ti-6Al-4V parts are illustrated in Figure 11 (optical micrographs) and Supplementary Figure 2 (scanning electron microscopy results). α′ is the white needle-shaped phase (see Supplementary Figure 2) and the matrix consists of α+β phase (Figure 11) known as the basket-weave phase [39]. Although the micrographs presented in Figure 11 and Supplementary Figure 2 were collected from samples with relative densities of > 99.8%, the variation of thermal history at different sample heights and the applied different energy density inputs were expected to impact the grain structure and phase evolution in the LB-PBF Ti-6Al-4V parts. In other words, manufactured parts showed different morphologies due to different heat inputs and cooling rates. When the cooling rate is high (~5600-6500°C/s in laser melting process [40]), the majority of β phase transforms to α′ phase, so the decomposition of α′ to α and β is suppressed due to high cooling rate (while temperature decreases to room temperature), however, a small fraction of β phase transforms to α phase directly after passing the β transus temperature. In contrast, for the cooling rates between ~2900 – 3600 °C/s[40], all of the β phase transforms to

α phase after passing the β transus temperature and none of the β phase transforms to α′. For cooling rates less than ~5600-6500 °C/s, as the cooling rate gets smaller, less amount of β phase transforms to α′ phase. Xu et al. [41] investigated the effect of process parameters on the final microstructure of LB-PBF parts. They reported that by decreasing energy density, the martensite phase can be preserved. In fact, the cumulative residence time of the previously deposited layer in a temperature range of >400°C decreased with the reduction of energy density, thus, the α′ martensite in the as-deposited Ti-6Al-4V alloy had limited time to decompose into α and β phases. Also, laser focal offset distance (FOD) had a direct impact on the final microstructure of the LB-PBF parts. Here, we showed when the FOD is zero (regardless of process parameters), the microstructure of the final parts are mainly comprised of acicular α′ martensitic phase with a minority of lamellar (α+β).

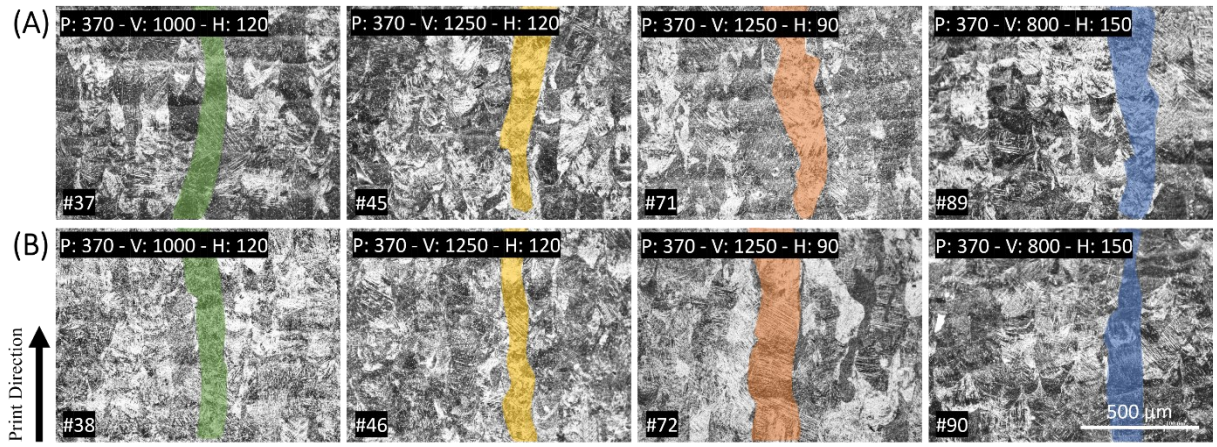


Figure 11. Optical micrographs taken from the LB-PBF processed HDH Ti-6Al-4V A) fine and B) coarse powders.

Supplementary Figure 2 illustrated SEM micrographs showing the dominance of the martensitic microstructure in the samples. By comparing samples #37 ($E$ = 51 J/mm$^3$, $H$ = 120 µm, $V$ = 1000 mm/s) and #89 ($E$ = 51 J/mm$^3$, $H$ = 150 µm and $V$ = 800 mm/s), it was seen that samples printed with the same energy density showed different α′ lath widths. Samples with smaller hatch spacings have more laser passes on the surface which leads to more high-temperature heating cycles. In other words, more heating cycles decrease the peak temperature. Lower peak temperature than martensitic start transformation temperature ($M_s$) results in coarsening of the existing martensitic features instead of decomposition of martensite because of insufficient dwell time and relatively lower peak temperature [42]. This point was also confirmed by comparing samples #45 ($H$ = 120 µm) and #71 ($H$ = 90 µm), in which larger martensite features were seen in sample #71. A similar trend was observed in the samples manufactured using the coarse powder. It appears that energy density can affect microstructure by changing the heat input and thermal history of the part, however, energy density is not a perfect criterion to produce the best final parts. For example, by doubling both laser power and scan speed the energy density will remain the same but the final part properties can be different. Prashanth et al. [29] reported different tensile properties of Al-12Si parts manufactured using the same energy density. They showed that the tensile properties of the parts are dependent on laser power, rather than energy density. Xu et al. [41] also observed when a constant energy density was applied on LB-PBF of Ti-6Al-4V using different combinations of laser power, scan speed, layer thickness, and FOD constant energy density, the final microstructure varied from fully acicular α′ martensite to mixed acicular α′ martensite and lamellar (α + β) which indicates that energy density is not a good criterion to rely

on. In other words, tuning the LB-PBF processing variables would lead to substantial variations in the constituent phases, owing to the changed thermal profiles.

Figure 12d Showed different microstructural features present in the LB-PBF Ti-6Al-4V parts. As mentioned before, martensite is the dominant phase in the as-build parts due to the high cooling rate of the LB-PBF process. Along with martensitic features, prior beta grain boundaries are visible. During the solidification process, all liquid phase inside the melt pool transforms to β phase, known as the prior beta phase, and this prior β phase then transforms directly to α′ martensite because of a high cooling rate. Since the martensite finish temperature ($M_f$) is below room temperature [37], a small amount of β phase remains between the α′ needles in the form of β nano particles, as reported by Oh et al. [43] and Y. Xu [44].

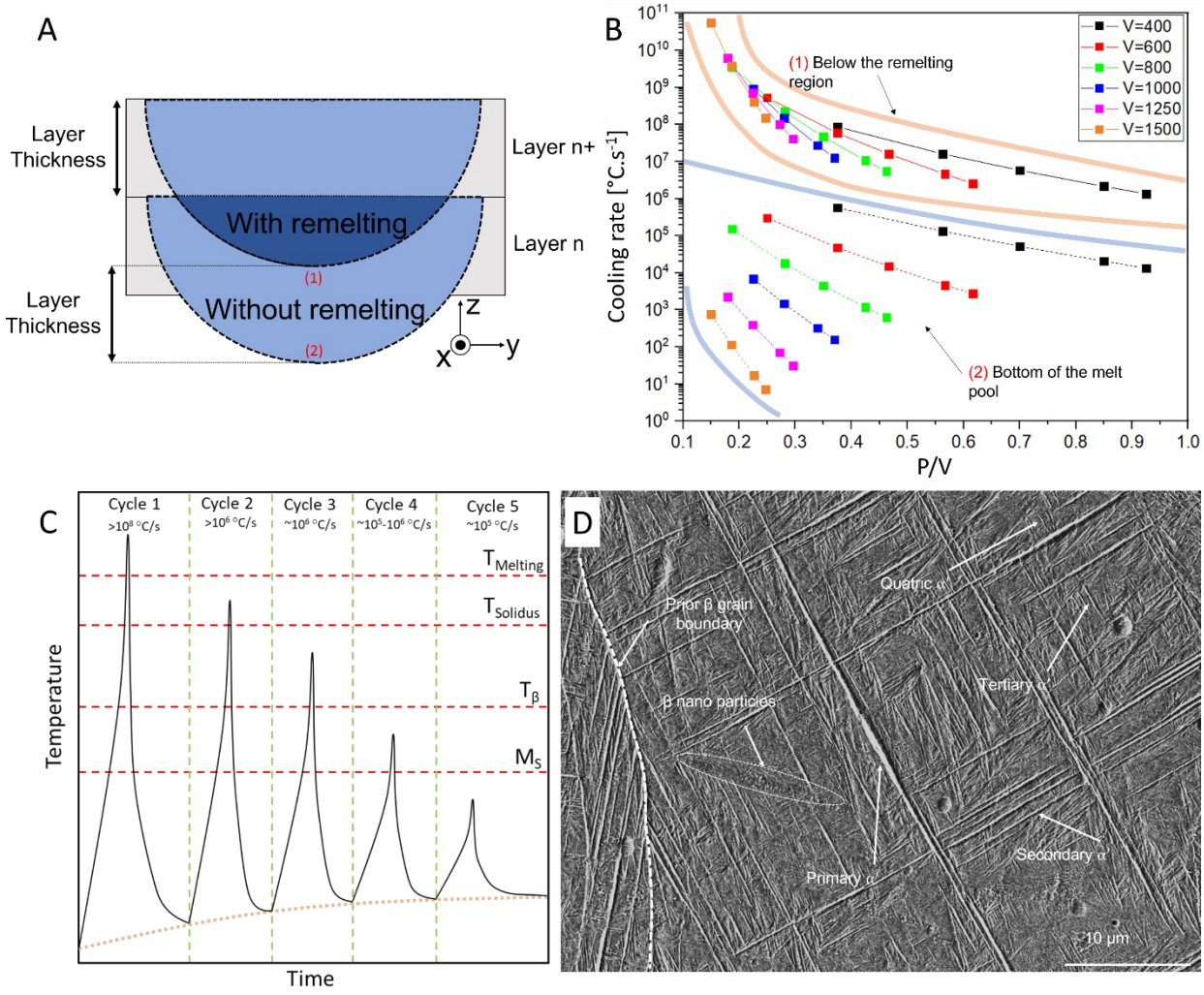


Figure 12. A) schematic of two consecutive layers showing the regions with and without remelting and B) Calculated cooling rates against P/V ratio. The region between orange curves shows the cooling rates just below the remelting region and the region between blue curves shows the cooling rates at the bottom of the melt pool. C) schematic representation of thermal cycles in the part because of laser passing on the surface and the corresponding estimated cooling rates and D) SEM micrograph of sample #37 showing different types of martensite features produced based on the heating cycles, β nano particles, and prior β grain boundary.

The amount of β nano particles is correlated with the cooling rate of the LB-PBF process which is affected by processing parameters. The cooling rate can be estimated using the following equation [45].

$$\frac{\partial T}{\partial t} = \left[1 + \frac{\xi}{\sqrt{\xi^2+z^2}} + \frac{2\alpha\xi}{V(\xi^2+z^2)}\right]\left(\frac{\lambda P}{2\pi k}\frac{V^2}{2\alpha}\frac{1}{\sqrt{\xi^2+z^2}}\right) EXP\left[-\frac{V}{2\alpha}\left(\xi + \sqrt{\xi^2+z^2}\right)\right] \quad \text{(Eq. 6)}$$

where $\xi$ is the relative distance to the center of the laser spot in the x-direction defined by $(x - Vt)$ (mm), $z$ is the vertical distance from the center of the laser spot (mm), $\alpha$ is the thermal diffusivity of Ti-6Al-4V alloy ($mm^2/s$), $V$ is the laser scan speed (mm/s), $P$ is the laser power (W), $k$ is the thermal conductivity of Ti-6Al-4V alloy (W/mm.K). Eq. 6 can be used to calculate the local cooling rate based on the laser power and scan speed at a certain distance from the laser spot. There is a penetration of the laser inside the previously deposited layer to fuse it to the new layer, therefore, there is an area of remelting in the previous layer. This remelting causes changes in the previously solidified region but there will be an area without remelting whose height will be equal to the layer thickness as shown in Figure 12a.

Depth of the melt pool changes based on the LB-PBF processing parameters; the depths were calculated using Eq. 2 and the calculated cooling rates at the bottom of the melt pool (point 2) and just below the remelting region (point 1) were plotted against the *P/V* ratio and the results were demonstrated in Figure 12b. The cooling rates decrease continuously with increasing *P/V* ratio despite the direct relationship between the cooling rate and laser power which is consistent with the results reported by Promoppatum et al [45] for Inconel 718 alloy. This happens because increasing laser power increases the melt pool depth, thus the region without remelting will be further away from the laser which will decrease the cooling rate because of the distance to the laser spot. On the other hand, the difference between the cooling rates at the bottom of the melt pool and below the remelting region increases as the *P/V* ratio decreases. This occurs because when the laser scan speed increases, there is less time for the temperature to become uniform throughout the melt pool; thus, with increasing laser scan speed, the temperature and the cooling rate at the bottom of the melt pool decrease. The average cooling rate inside the region without remelting is well above the range (~5600-6500°C/s) of obtaining fully martensitic microstructure, thus, the microstructure of the mentioned area is fully martensitic after solidification and before deposition of the next layer as reported by Vaglio et al [46] with single-track experiments on Ti-6Al-4V alloy. They showed that the microstructure of the single tracks will be fully martensitic regardless of the processing parameters.

Although the effect of laser power and scan speed is obvious on the cooling rates, it should be mentioned that the thermal cycles in the part play a role in determining the final microstructure of the LB-PBF Ti-6Al-4V part. With each pass of the laser on the surface, thermal cycles inside the fabricated part will cause a small amount of α′ to be decomposed into α+β as shown in Figure 12d. The peak temperature of each thermal cycle in a specific coordinate decreases as the subsequent layers are being deposited and the assumption is that every point inside the part experiences the same heat cycles as reported by various studies [42,47]. Figure 12c schematically shows the peak temperatures during each thermal cycle. The first peak is well above the melting temperature of the Ti-6Al-4V alloy with the cooling rate calculated and shown in Figure 12b. The second peak is above the solidus temperature, thus, the specific location undergoing this cycle experiences a slight local melting and fully β phase coexist with liquid, however, because the cooling rate is still more than ~$10^6$ °C/s, the microstructure is fully martensitic but the martensite features from this cycle are more refined. They are the secondary α′ that coexist with the primary α′. As the peak temperature of the third cycle is above the β transus, all of the martensitic features transform to β

phase but still some of the dislocations from the decomposed α′ will remain because of high heating rate which act as nucleation points for the new martensitic features [48]. During the fourth cycle, the peak temperature is below β transus, thus, some of the small martensitic features decompose to β phase but the primary α′ features remain untouched because of insufficient dwelling time in that temperature as reported by Qazi et al [49], and the β phase transforms into even more refined α′ features called tertiary α′. In the fifth cycle, local transformation to β phase occurs and because of the high cooling rate, those β phases transform into quatric α′. In the next heating cycles, small amounts of α′ decompose into β phase and form the β nano particles shown in Figure 12d.

Figure 13 showed the effect of laser scan speed on microstructural evolution of LB-PBF Ti-6Al-4V parts manufactured using constant laser power of 370 W and different laser scan speeds in the range of 400 mm/s to 1500 mm/s. A lower scan speed of 400 mm/s (sample #9) resulted in a combination of short columnar and a considerable number of equiaxed grains. Increasing laser scan speed to 800 mm/s (sample #29) decreased the number of equiaxed grains along with preserving the columnar grains. A laser scan speed of 1000 mm/s can be considered as the critical scan speed in which all the equiaxed grains are removed and only columnar grains are visible. The presence of equiaxed grains can be explained by lower cooling rate because of lower laser scan speed based on Eq. (6) and lack of new nuclei introduced in the melt pool. Wu et al. [50] reported the same phenomenon in the DLF processed Ti-6Al-4V samples.

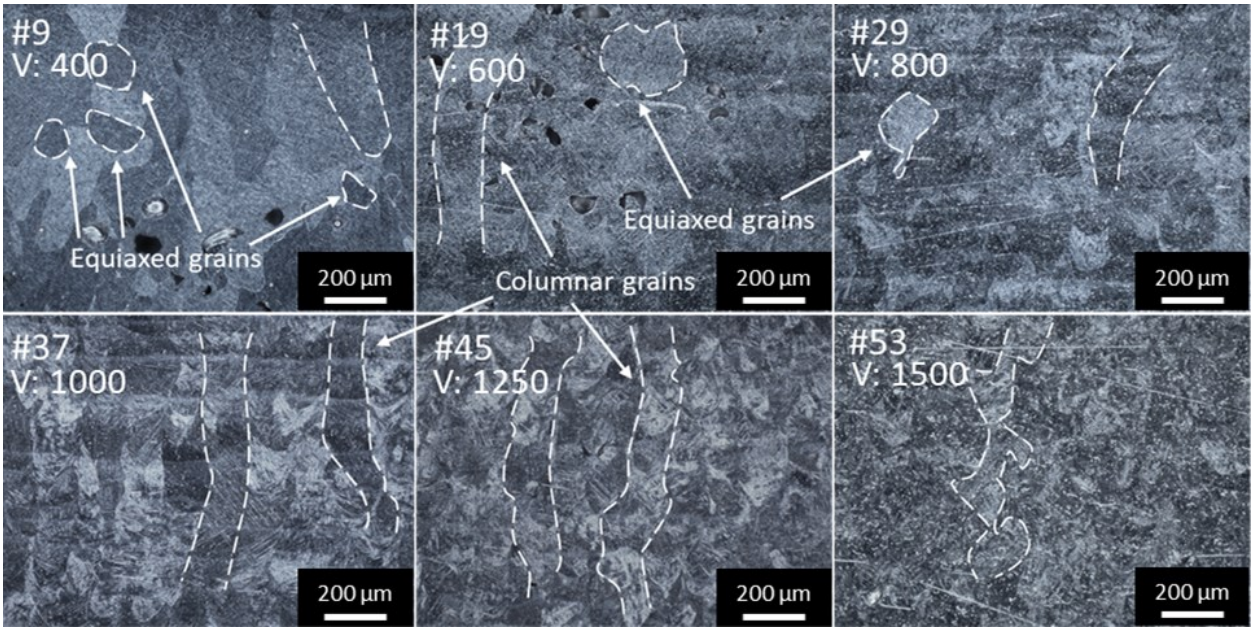


Figure 13. Optical micrographs of LB-PBF Ti-6Al-4V parts manufactured with laser power of 370 W and different laser scan speed of 400 to 1500 mm/s as indicated in each micrograph. Micrographs were collected from the near top surface region of the samples.

Further increasing laser scan speeds resulted in the distortion of columnar grain boundaries. The higher speed also increases the melt pool instability, thus, disrupting continuous epitaxial grain growth in the material and leading to distortion of grain boundaries. As suggested by Wang et al. [51], increasing laser scan speed results in a higher temperature at the edges of the melt pool compared to the bottom of it, thus, epitaxial growth of the grain is distorted.

Pauza et al. [52] modeled the microstructure development in LB-PBF and showed that the shape of the melt pool plays an important role in determining the final microstructure of the part which is consistent with the results in the present study. Relatively slower laser scan speed (400 –

800 mm/s) results in a deeper melt pool with the shape of a keyhole and a higher rate of instability and non-uniform thermal gradient which results in grain growth and equiaxed grains in the previously deposited layers. Increasing laser scan speed reduces the penetration time of laser and results in the semi-elliptical shape of the melt pool which is more stable and has enough penetration to completely fuse the new layer to the previously deposited layer and increases the chance of regrowth in grains, thus, grains in the parts produced with a laser scan speed of 1000 – 1250 mm/s showed more uniform shape. Further increasing the laser scan to 1500 mm/s results in a shallow semicircular shaped melt pool which decreases the chance of grain regrowth, thus, the distortion of grain boundaries occurs.

### *3.8 Dynamic x-ray radiography*

Dynamic x-ray radiography is an attenuation-based x-ray technique meaning the differences in laser absorptions and material densities result in contrast. As highlighted in Figure 14a-c, the darker regions are the solid phases, i.e., the powder and metal substrate, and the lighter regions are the gas phases, i.e., the vapor cavity and ambient argon environment. Figure 9B shows that the builds using the coarse and the fine HDH powders displayed different sensitivity to the variation of laser energy density especially when the energy level is suboptimal. This trend motivated the use of *in-situ* x-ray imaging technique to observe the interaction between the powder and the laser. The findings assist in understanding how powder size and morphological irregularity may influence laser melting at keyhole mode by comparing the experiments conducted in three different powder beds, i.e., the spherical gas atomized powder and the coarse and fine HDH powders. The laser parameter set of 350 W and 700 mm/s was selected since this parameter set is on the verge of the transition to the unstable keyhole regime where the observable keyhole size is maximized while no formation of keyhole porosity interrupts the measurements of keyhole depth.

Figure 14d summarizes the profiles of the melt pool depth as a function of laser melting time. The average keyhole depths are 261.4 ± 17.4 μm for the gas atomized powder, 248.2 ± 14.8 μm for the fine HDH powder, and 247.7 ± 22.5 μm for the coarse HDH powder. Note that the important difference is not the average depths, since it could be affected by the variation of layer thickness, but the standard deviations which reflect the severity of the keyhole fluctuation in the presence of different powders. The keyhole fluctuation is clearly more severe in the coarse HDH powder bed. Surprisingly, the fine HDH powder bed resulted in the mildest fluctuation among the three experiments. Figure 14a-c shows the most intense keyhole fluctuation in all three experiments where porosity formation events were observed more frequently in the coarse HDH powder bed. The larger fluctuation can be attributed to the amplification of the laser shadowing effect in the HDH powder bed as suggested in our previous effort [17]. When the laser is shadowed by a HDH particle, the local cooling is expected to last longer due to the larger particle size. Once the laser path is fully restored, the substrate is often more exposed since the powder layer of the coarse HDH powder possesses lower counts of particles compared with the other powder beds as shown in Figure 14a-c. As the result, both the shrinkage and the expansion of the keyhole are amplified. As shown in Figure 14e, a similar trend was observed in the keyhole width measurements where the standard deviations of width are 29.0 μm for the coarse HDH powder, 24.2 μm for the fine HDH powder, and 24.1 μm for the gas atomized powder. Reducing particle size appeared to be effective to mitigate the violent fluctuation as the fine HDH powder behaved more similarly to the spherical gas atomized powder. It is believed that the smaller particle size of the fine HDH powder bed helped reduce the keyhole fluctuation. The result suggests that it may

be feasible to control keyhole behaviors through only altering particle size without eliminating the powder shape irregularity.

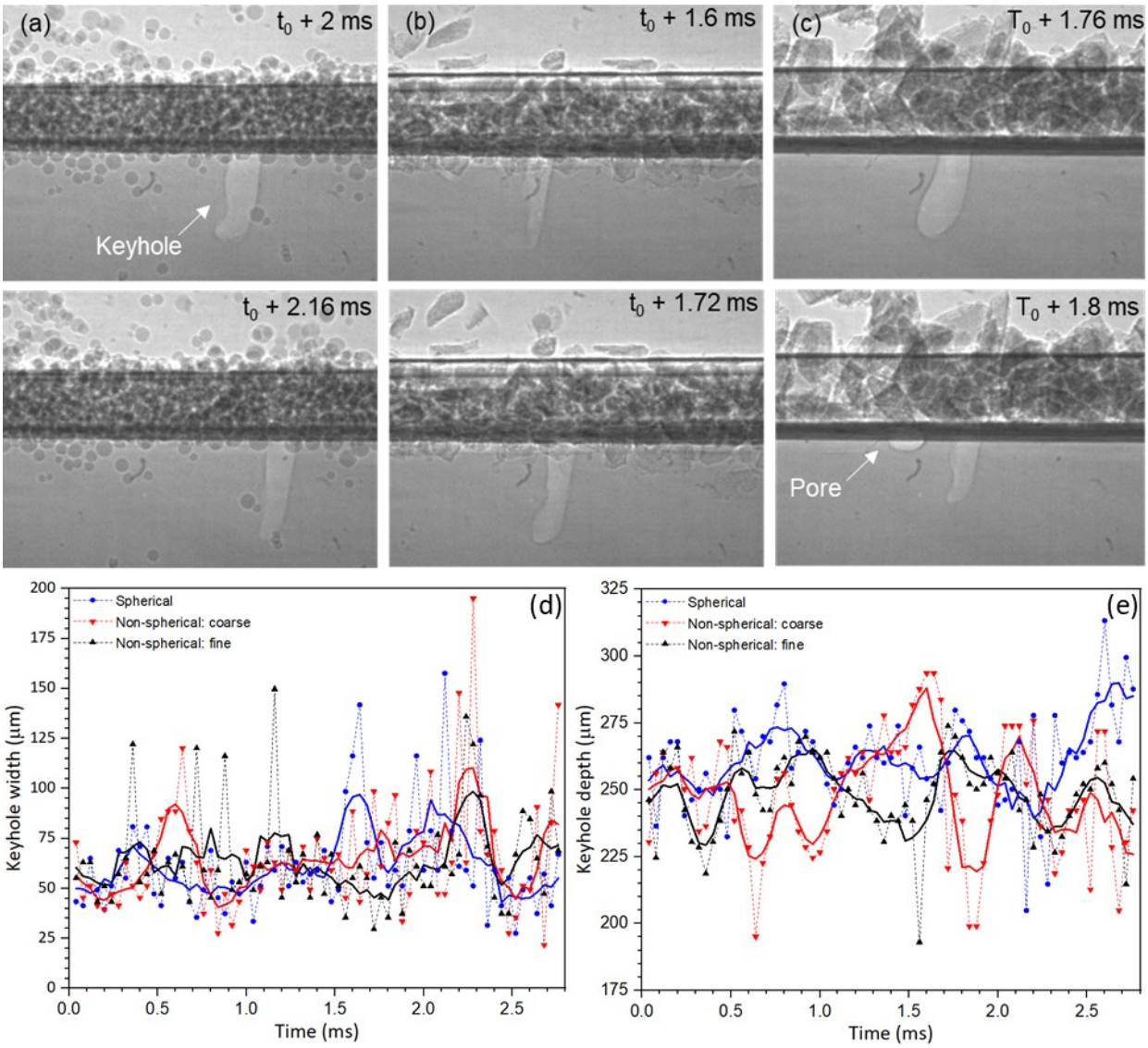


Figure 14. DXR frames collected in the (a) gas atomized, (b) fine HDH powder, and (c) coarse HDH powder added single-bead Ti-6Al-4V experiments at a laser power of 350 W and a scan speed of 700 mm/s showing the fluctuations of keyhole dimensions. The keyhole depth profiles and the width profiles are shown in (d) and (e). Note that the timestamps in (a-c) are the time since the laser was initiated. The DXR videos (Supplementary Video S1, S2, and S3) can be found in the supplementary material. Bold solid lines in (d) and (e) are 5 point moving averages.

### 3.9 *Vickers microhardness*

The microhardness tests were carried out on samples manufactured using fine HDH powder, at a hatch spacing of 120 μm, and various laser power and scan speeds and the results were shown in Figure 15. Increasing laser scan speed while keeping the laser power (P = 370 W) constant, causes the hardness to increase up to laser scan speed of 1250 mm/s and decrease in hardness by further increase in laser scan speed. This phenomenon can be correlated with the columnar prior β grains morphology as discussed before (see Figure 13). Also, increase in laser power with constant laser scan speed (V = 1250 mm/s) results in higher hardness due to mainly decrease in porosity

content. However, the inverse correlation between the hardness and laser power in the low laser scan speed region (V = 400 or 600 mm/s) was spotted. This can be explained by the fact the increasing laser power in this region results in change in pore formation mechanism at first (from P = 150 to P = 225 W) and increase in pore size with further increase of laser power. Micro-hardness indent has less probability of contacting larger LoF pores with higher distance between them compared to circular keyhole pores that are more uniformly spread throughout the sample. Results were in agreement of the reported values for LB-PBF Ti-6Al-4V alloy [15,53].

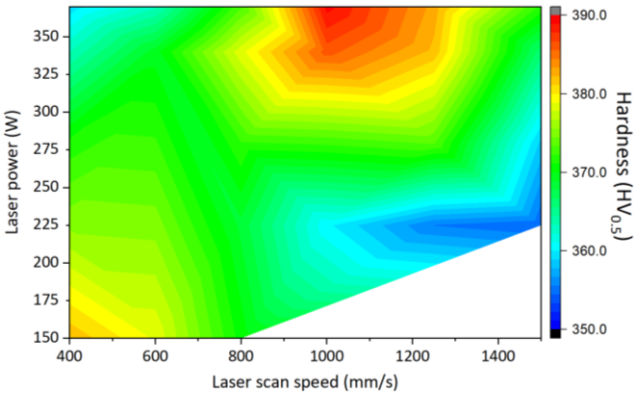


Figure 15. Vickers microhardness variation based on the processing parameters of the LB-PBF processed Ti-6Al-4V alloy. Data was collected on the samples manufactured using fine powder with a constant hatch spacing of 120 µm.

## 4. Conclusions

This study was carried out to show the successful utilization of cost-effective non-spherical HDH Ti-6Al-4V powders in the LB-PBF process to lower the cost of production compared to the use of GA powders. Below are the major findings:

- Despite the possibility of mechanical interlocking between powder particles, HDH powders (both fine and coarse powders with PSD of 50-120 µm and 75-175 µm, respectively) showed better flowability compared to GA powders with 20-63 µm size distribution. This better powder flow of the HDH powder is most easily accounted for by the powder size since coarse powder (e.g., HDH powder with $D_{50}$ > 50 µm) is known to flow better than fine ones (e.g., GA powder with $D_{50}$ < 35 µm). By using optimized process parameters, samples with a relative density of >99.5% were manufactured.
- The micro-computed tomography analysis showed the overall packing density of the fine and coarse HDH powders was 54.8 % and 53.9 %, respectively. Similar to the coarse HDH powder, the fine HDH powder also has many low-density packing spots, proven by the Monte Carlo analysis, with 20 % - 40 % packing fraction at nominal LB-PBF melt pool sizes.
- Parts with a relative density of >99.5 % were produced using a build rate of 1.5-2 times of the nominal production rate and lower energy density (30-60 J/mm$^3$ in HDH powder) compared to GA powders and standard EOS M290 parameters (~75 J/mm$^3$). By increasing the build rate, parts are produced faster using less energy which will lower the cost of production even further.
- Microstructure and phase analysis indicated that acicular α′ martensite was the main phase in LB-PBF Ti-6Al-4V parts owing to the high cooling rates. Traces fractions of β phase (about 1-4 %) with nano-granular morphology were also detected despite the extremely high cooling rate during solidification of the melt pool.
- Grain morphology in LB-PBF Ti-6Al-4V parts changed from regional equiaxed to fully columnar and then distorted columnar by increasing laser scan speed at a constant laser power.

The change in grain morphology occurred because of melt pool shape change and heat transfer disturbance which affect the chance of grain regrowth and new grains nucleation.

- *In situ synchrotron* x-ray imaging showed that coarse HDH powder (75-175 μm) caused less packing density and higher laser shadowing effect which resulted in higher variation in keyhole depth. Fine HDH powder (50-125 μm) behaved similar to GA powder (20-63 μm), both in keyhole depth and width fluctuations. This suggests that, by using non-spherical powder with an optimized PSD, laser shadowing can be mitigated.
- Mechanical testing showed dependency of Vickers microhardness to process parameters and resultant microstructure of the LB-PBF Ti-6Al-4V in which the highest value of ~390 $HV_{0.5}$ was attained for samples with a density of > 99.8%.

## Acknowledgments

AM would like to acknowledge the startup funding from the Department of Mechanical, Materials and Aerospace Engineering and Armour College of Engineering at Illinois Institute of Technology at Chicago, Illinois. This work is supported, in part, by the Pennsylvania Infrastructure Technology Alliance, a partnership of Carnegie Mellon, Lehigh University, and the Commonwealth of Pennsylvania's Department of Community and Economic Development (DCED). The authors recognize Reading Alloys (formerly affiliated with AMETEK Inc., now a part of Kymera International) for providing the powder used in this work. The authors acknowledge the support of the NextManufacturing Center and the use of the Materials Characterization Facility, supported by grant MCF-677785, at Carnegie Mellon University. This research used resources of the Advanced Photon Source, a US Department of Energy (DOE) Office of Science User Facility operated for the DOE Office of Science by Argonne National Laboratory under Contract No. DE-AC02-06CH11357 in addition to supporting through Laboratory Directed Research and Development (LDRD) funding from Argonne National Laboratory under the same contract. Dr. Tao Sun, Dr. Niranjan Parab, Dr. Cang Zhao, and all the 32-ID beamline staff at the Advanced Photon Source are thanked for assisting in the acquisition of the DXR data. Undergraduate student researchers (EG and SF) were supported by the National Science Foundation - Research Experience for Undergraduates under award DMR 2050916.

## References

[1] W. Ding, G. Chen, M. Qin, Y. He, X. Qu, Low-cost Ti powders for additive manufacturing treated by fluidized bed, Powder Technol. 350 (2019) 117–122.

[2] W. Ding, Z. Wang, G. Chen, W. Cai, C. Zhang, Q. Tao, X. Qu, M. Qin, Oxidation behavior of low-cost CP-Ti powders for additive manufacturing via fluidization, Corros. Sci. 178 (2021) 109080.

[3] Y.P. Dong, Y.L. Li, S.Y. Zhou, Y.H. Zhou, M.S. Dargusch, H.X. Peng, M. Yan, Cost-affordable Ti-6Al-4V for additive manufacturing: Powder modification, compositional modulation and laser in-situ alloying, Addit. Manuf. (2020) 101699.

[4] M.J. Donachie, Titanium : a technical guide, (2000).

[5] G. Chen, S.Y. Zhao, P. Tan, J. Wang, C.S. Xiang, H.P. Tang, A comparative study of Ti-6Al-4V powders for additive manufacturing by gas atomization, plasma rotating electrode process and plasma atomization, Powder Technol. 333 (2018) 38–46.

[6] Y.Y. Sun, S. Gulizia, C.H. Oh, C. Doblin, Y.F. Yang, M. Qian, Manipulation and Characterization of a Novel Titanium Powder Precursor for Additive Manufacturing Applications, JOM. 67 (2015) 564–572.

[7] W. Ding, G. Chen, M. Qin, Y. He, X. Qu, Low-cost Ti powders for additive manufacturing treated by fluidized bed, Powder Technol. 350 (2019) 117–122.

[8] S.P. Narra, Z. Wu, R. Patel, J. Capone, M. Paliwal, J. Beuth, A. Rollett, Use of Non-Spherical Hydride-Dehydride (HDH) Powder in Powder Bed Fusion Additive Manufacturing, Addit. Manuf. 34 (2020) 101188.

[9] A. Rogalsky, I. Rishmawi, L. Brock, M. Vlasea, Low cost irregular feed stock for laser powder bed fusion,

J. Manuf. Process. 35 (2018) 446–456.
[10] R. Cunningham, A. Nicolas, J. Madsen, E. Fodran, E. Anagnostou, M.D. Sangid, A.D. Rollett, Analyzing the effects of powder and post-processing on porosity and properties of electron beam melted Ti-6Al-4V, Mater. Res. Lett. 5 (2017) 516–525.
[11] N.D. Parab, J.E. Barnes, C. Zhao, R.W. Cunningham, A.D. Rollett, T. Sun, Real time observation of binder jetting printing process using high-speed X-ray imaging, Sci. Rep. (2019) 28–30.
[12] A. Mostafaei, C. Zhao, Y. He, S. Reza Ghiaasiaan, B. Shi, S. Shao, N. Shamsaei, Z. Wu, N. Kouraytem, T. Sun, J. Pauza, J. V. Gordon, B. Webler, N.D. Parab, M. Asherloo, Q. Guo, L. Chen, A.D. Rollett, Defects and anomalies in powder bed fusion metal additive manufacturing, Curr. Opin. Solid State Mater. Sci. 26 (2022) 100974.
[13] F. Medina, Reducing metal alloy powder costs for use in powder bed fusion additive manufacturing: Improving the economics for production, The University of Texas at El Paso, 2013.
[14] R. Li, Y. Shi, Z. Wang, L. Wang, J. Liu, W. Jiang, Densification behavior of gas and water atomized 316L stainless steel powder during selective laser melting, Appl. Surf. Sci. 256 (2010) 4350–4356.
[15] J. Varela, E. Arrieta, M. Paliwal, M. Marucci, J.H. Sandoval, J.A. Gonzalez, B. McWilliams, L.E. Murr, R.B. Wicker, F. Medina, Investigation of Microstructure and Mechanical Properties for Ti-6Al-4V Alloy Parts Produced Using Non-Spherical Precursor Powder by Laser Powder Bed Fusion, Materials (Basel). 14 (2021) 3028.
[16] ASTM B348: Standard Specification for Titanium and Titanium Alloy Bars and Billets, Vol 02.04, (n.d.).
[17] Z. Wu, M. Asherloo, R. Jiang, M.H. Delpazir, N. Sivakumar, M. Paliwal, J. Capone, B. Gould, A. Rollett, A. Mostafaei, Study of Printability and Porosity Formation in Laser Powder Bed Fusion Built Hydride-Dehydride (HDH) Ti-6Al-4V, Addit. Manuf. (2021).
[18] C.A. Schneider, W.S. Rasband, K.W. Eliceiri, NIH Image to ImageJ: 25 years of image analysis, Nat. Methods. 9 (2012) 671–675.
[19] L. Scime, Methods for the Expansion of Additive Manufacturing Process Space and the Development of In-Situ Process Monitoring Methodologies, Carnegie Mellon Univ. (2018).
[20] I. Yadroitsev, I. Yadroitsava, 3 - A step-by-step guide to the L-PBF process, in: I. Yadroitsev, I. Yadroitsava, A. du Plessis, E.B.T.-F. of L.P.B.F. of M. MacDonald (Eds.), Addit. Manuf. Mater. Technol., Elsevier, 2021: pp. 39–77.
[21] R. Al-Raoush, K.A. Alshibli, Distribution of local void ratio in porous media systems from 3D X-ray microtomography images, Phys. A Stat. Mech. Its Appl. 361 (2006) 441–456.
[22] K.F. H., P. Dayakar, G. Jens, K. Nikolay, M. Ingo, High-Resolution Neutron and X-Ray Imaging of Granular Materials, J. Geotech. Geoenvironmental Eng. 139 (2013) 715–723.
[23] R. Russell, D. Wells, J. Waller, B. Poorganji, E. Ott, T. Nakagawa, H. Sandoval, N. Shamsaei, M. Seifi, Qualification and certification of metal additive manufactured hardware for aerospace applications, Elsevier Inc., 2019.
[24] E. Wycisk, A. Solbach, S. Siddique, D. Herzog, F. Walther, C. Emmelmann, Effects of defects in laser additive manufactured Ti-6Al-4V on fatigue properties, Phys. Procedia. 56 (2014) 371–378.
[25] M. Tang, P.C. Pistorius, J.L. Beuth, Prediction of lack-of-fusion porosity for powder bed fusion, Addit. Manuf. 14 (2017) 39–48.
[26] H. Gong, K. Rafi, H. Gu, T. Starr, B. Stucker, Analysis of defect generation in Ti-6Al-4V parts made using powder bed fusion additive manufacturing processes, Addit. Manuf. 1 (2014) 87–98.
[27] T. Mukherjee, T. DebRoy, Mitigation of lack of fusion defects in powder bed fusion additive manufacturing, J. Manuf. Process. 36 (2018) 442–449.
[28] S. Coeck, M. Bisht, J. Plas, F. Verbist, Prediction of lack of fusion porosity in selective laser melting based on melt pool monitoring data, Addit. Manuf. 25 (2019) 347–356.
[29] K.G. Prashanth, S. Scudino, T. Maity, J. Das, J. Eckert, Is the energy density a reliable parameter for materials synthesis by selective laser melting?, Mater. Res. Lett. 5 (2017) 386–390.
[30] C. Zhao, N.D. Parab, X. Li, K. Fezzaa, W. Tan, A.D. Rollett, T. Sun, Critical instability at moving keyhole tip generates porosity in laser melting, Science (80-. ). 1086 (2020) 1080–1086.
[31] D. Rosenthal, Mathematical theory of heat distribution during welding and cutting, Weld. J. 20 (1941) 220–234.
[32] G. Welsch, R. Boyer, E.W. Collings, Materials Properties Handbook: Titanium Alloys, ASM International, 1993.
[33] R. Cunningham, C. Zhao, N. Parab, C. Kantzos, J. Pauza, K. Fezzaa, T. Sun, A.D. Rollett, Keyhole Threshold and Morphology in Laser Melting Revealed by Ultrahigh- Speed X-ray Imaging, Science (80-. ). 363 (2019) 849–852.

[34] L. Thijs, F. Verhaeghe, T. Craeghs, J. Van Humbeeck, J.P. Kruth, A study of the microstructural evolution during selective laser melting of Ti-6Al-4V, Acta Mater. 58 (2010) 3303–3312.
[35] R. Boyer, G. Welsch, E.W. Collings, Materials Properties Handbook: Titanium Alloys, ASM International, Materials Park, OH, 1994, There Is No Corresp. Rec. This Ref. Sch. (n.d.).
[36] L.E. Murr, S.A. Quinones, S.M. Gaytan, M.I. Lopez, A. Rodela, E.Y. Martinez, D.H. Hernandez, E. Martinez, F. Medina, R.B. Wicker, Microstructure and mechanical behavior of Ti–6Al–4V produced by rapid-layer manufacturing, for biomedical applications, J. Mech. Behav. Biomed. Mater. 2 (2009) 20–32.
[37] S. Liu, Y.C. Shin, Additive manufacturing of Ti6Al4V alloy: A review, Mater. Des. 164 (2019) 107552.
[38] C.M. Cepeda-Jiménez, F. Potenza, E. Magalini, V. Luchin, A. Molinari, M.T. Pérez-Prado, Effect of energy density on the microstructure and texture evolution of Ti-6Al-4V manufactured by laser powder bed fusion, Mater. Charact. 163 (2020) 110238.
[39] J. Sieniawski, Microstructure and Mechanical Properties of High Strength Two-Phase Titanium Alloys, in: W. Ziaja (Ed.), IntechOpen, Rijeka, 2013: p. Ch. 4.
[40] S.A. Oh, R.E. Lim, J.W. Aroh, A.C. Chuang, B.J. Gould, B. Amin-Ahmadi, J. V. Bernier, T. Sun, P.C. Pistorius, R.M. Suter, A. D.Rollett, High speed synchrotron X-ray diffraction experiments resolve microstructure and phase transformation in laser processed Ti-6Al-4V, Mater. Res. Lett. 9 (2021) 429–436.
[41] W. Xu, M. Brandt, S. Sun, J. Elambasseril, Q. Liu, K. Latham, K. Xia, M. Qian, Additive Manufacturing of Strong and Ductile Ti-6Al-4V by Selective Laser Melting via In Situ Martensite Decompisition, Acta Mater. 85 (2015) 74–84.
[42] J. Yang, H. Yu, J. Yin, M. Gao, Z. Wang, X. Zeng, Formation and control of martensite in Ti-6Al-4V alloy produced by selective laser melting, Mater. Des. 108 (2016) 308–318.
[43] S.A. Oh, R.E. Lim, J.W. Aroh, A.C. Chuang, B.J. Gould, B. Amin-Ahmadi, J. V. Bernier, T. Sun, P.C. Pistorius, R.M. Suter, A. D.Rollett, High speed synchrotron X-ray diffraction experiments resolve microstructure and phase transformation _ Enhanced Reader.pdf, MATER. RES. LETT. 9 (2021) 429–436.
[44] Y. Xu, Corrosion Behavior of Direct Metal Laser Sintered Ti-6Al-4V for Orthopedic Applications, 2021.
[45] P. Promoppatum, S.C. Yao, P.C. Pistorius, A.D. Rollett, A Comprehensive Comparison of the Analytical and Numerical Prediction of the Thermal History and Solidification Microstructure of Inconel 718 Products Made by Laser Powder-Bed Fusion, Engineering. 3 (2017) 685–694.
[46] E. Vaglio, T. De Monte, A. Lanzutti, G. Totis, M. Sortino, L. Fedrizzi, Single tracks data obtained by selective laser melting of Ti6Al4V with a small laser spot diameter, Data Br. 33 (2020) 106443.
[47] C.H. Fu, Y.B. Guo, Three-dimensional temperature gradient mechanism in selective laser melting of Ti-6Al-4V, J. Manuf. Sci. Eng. 136 (2014).
[48] O.M. Ivasishin, R. V Teliovich, Potential of rapid heat treatment of titanium alloys and steels, Mater. Sci. Eng. A. 263 (1999) 142–154.
[49] J.I. Qazi, O.N. Senkov, J. Rahim, F.H. Froes, Kinetics of martensite decomposition in Ti-6Al-4V-xH alloys, Mater. Sci. Eng. A. 359 (2003) 137–149.
[50] X. Wu, J. Liang, J. Mei, C. Mitchell, P.S. Goodwin, W. Voice, Microstructures of laser-deposited Ti–6Al–4V, Mater. Des. 25 (2004) 137–144.
[51] Z. Wang, Z. Xiao, Y. Tse, C. Huang, W. Zhang, Optimization of processing parameters and establishment of a relationship between microstructure and mechanical properties of SLM titanium alloy, Opt. Laser Technol. 112 (2019) 159–167.
[52] J.G. Pauza, W.A. Tayon, A.D. Rollett, Computer simulation of microstructure development in powder-bed additive manufacturing with crystallographic texture, Model. Simul. Mater. Sci. Eng. 29 (2021) 55019.
[53] A.E. Wilson-Heid, Z. Wang, B. McCornac, A.M. Beese, Quantitative relationship between anisotropic strain to failure and grain morphology in additively manufactured Ti-6Al-4V, Mater. Sci. Eng. A. 706 (2017) 287–294.